Inorganic Chemistry
Cite This: Inorg. Chem. 2019, 58, 11636−11648
Article
pubs.acs.org/IC

Rare-Earth and Antimony-Oxo Clusters Simultaneously Connecting Antimonotungstates Comprising Divacant and Tetravacant Keggin Fragments

Xin Xu, Yanhong Chen, Yan Zhang, Yifan Liu, Lijuan Chen,* and Junwei Zhao*

Henan Key Laboratory of Polyoxometalate Chemistry, College of Chemistry and Chemical Engineering, Henan University, Kaifeng, Henan 475004, China

Supporting Information

ABSTRACT: Four novel rare-earth (RE) and Sb-oxo clusters simultaneously bridging antimonotungstates (ATs) $[H_2N(CH_3)_2]_8Na_6H_8\{[RE_4(H_2O)_6Sb_6O_4](SbW_{10}O_{37})_2(SbW_8O_{31})_2\}\cdot 24H_2O$ [RE = Dy^{3+} (**1**), Er^{3+} (**2**), Y^{3+} (**3**), Ho^{3+} (**4**)] were triumphantly isolated by using $Na_9[B\text{-}\alpha\text{-}SbW_9O_{33}]\cdot 19.5H_2O$, dimethylamine hydrochloride, $SbCl_3$, and $RE(NO_3)_3\cdot 6H_2O$ in acidic aqueous solution. Their tetrameric polyoxoanions are all established by two $[SbW_{10}O_{37}]^{11-}$ and two $[B\text{-}\alpha\text{-}SbW_8O_{31}]^{11-}$ segments encapsulating a RE-Sb heterometal $[RE_4(H_2O)_6Sb_6O_4]^{22+}$ cluster. Under the O→W LMCT excitation at 268 nm of AT segments, RE ions in **1** and **2** can absorb the $^3T_{1u}\rightarrow{}^1A_{1g}$ emission energy of AT segments, giving rise to the sensitization of AT segments to the emission of RE ions. Through the sensitization of AT segments, the emission intensities of RE ions in **1** and **2** are increased and lifetimes are prolonged. Photoluminescence and energy transfer measurements indicate that Dy^{3+} ions in **1** can obtain more energy from AT segments than to Er^{3+} ions in **2**. Furthermore, the sensitization effects of AT segments to different *f*−*f* transitions of RE ions have been compared in **1** and **2**. Under the sensitization of AT segments, the $^4F_{9/2}\rightarrow{}^6H_{15/2}$ transition obtains the most energy compared with the $^4F_{9/2}\rightarrow{}^6H_{13/2}$ and $^4F_{9/2}\rightarrow{}^6H_{11/2}$ transitions in **1**, and the $^2H_{11/2}\rightarrow{}^4I_{15/2}$ transition obtains more energy than the $^4S_{3/2}\rightarrow{}^4I_{15/2}$ transition in **2**. It seems that the better energy level match of $^3T_{1u}\rightarrow{}^1A_{1g}$ transition of AT segments with *f*−*f* emission transitions of RE ions will lead to a stronger sensitization effect.

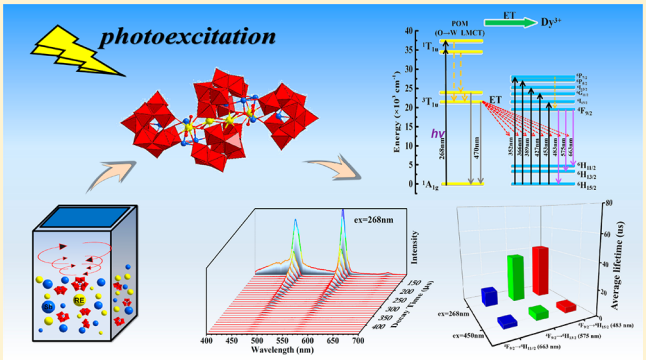

INTRODUCTION

Polyoxometalates (POMs) have well-known as early transition metal−oxygen clusters for approximately two centuries. They exhibit characteristic architectures and various compositions as well as having potential applications in catalysis, magnetism, electroanalytical chemistry, bioagnostic pharmacy, nonlinear optics, and so on.[1−11] Because of their features of maintaining stability and integrity in solid or solution, owning large oxygen-enriched surfaces, and displaying interesting electronic properties, POMs can perform as multidentate inorganic ligands, especially for lacunary POMs with defined vacancies in the skeletons.[3,12−15] Plenary Keggin-type heteropolyoxotungstate (HPOT) anions can lose three $\{WO_6\}$ octahedra and generate representative trilacunary HPOT segments involving $[XW_9O_{33}]^{n-}$ (X = Se^{IV}, Te^{IV}, *n* = 8, As^{III}, Sb^{III}, Bi^{III}, *n* = 9) segments with the lone-pair electrons and $[XW_9O_{34}]^{n-}$ (X = P^V, As^V, *n* = 9; Si^{IV}, Ge^{IV}, *n* = 10) segments without the lone-pair electrons.[16] Lacunary HPOT segments possess some advantages: (i) they bear high surface negative charges; (ii) they have excellent affinity toward various kinds of electrophiles, such as transition-metal (TM) ions, rare-earth (RE) ions, and main group (MG) ions, owning to the existence of nucleophilic oxygen centers at the vacant sites;[17] and (iii) they function as superior inorganic building blocks with various sizes, shapes, solubility, flexible coordination sites, and modes.[18,19] Therefore, designing and developing novel HPOT-based materials is feasible by means of a suitable reaction strategy of combing trivacant Keggin-type HPOT segments with other appropriate functional components.[20]

In the HPOT family, antimonotungstate (AT) chemistry based on trivacant Keggin $[B\text{-}\alpha\text{-}SbW_9O_{33}]^{9-}$ subunits has developed as a significant subclass with numerous innovative structures and potential applications. Compared to other HPOT subclasses such as $[PW_9O_{34}]^{9-}$, $[AsW_9O_{33}]^{9-}$, and $[GeW_9O_{34}]^{10-}$, the AT family based on $[SbW_9O_{33}]^{9-}$ subunits is less explored, which provides an appreciable development prospect.[21] Through literature investigations, it can be found that investigations on the AT family have been concentrated on TM-substituted AT species, whereas reports on RE and TM-RE-substituted ATs are very limited, and only several typical examples have been reported.[22−26] Furthermore, the empty 5s and 5p orbitals of the main-group Sb^{3+} ion can also perform as effective metal linkers. Examples of introducing

Received: May 28, 2019
Published: August 15, 2019

DOI: 10.1021/acs.inorgchem.9b01570
Inorg. Chem. 2019, 58, 11636−11648

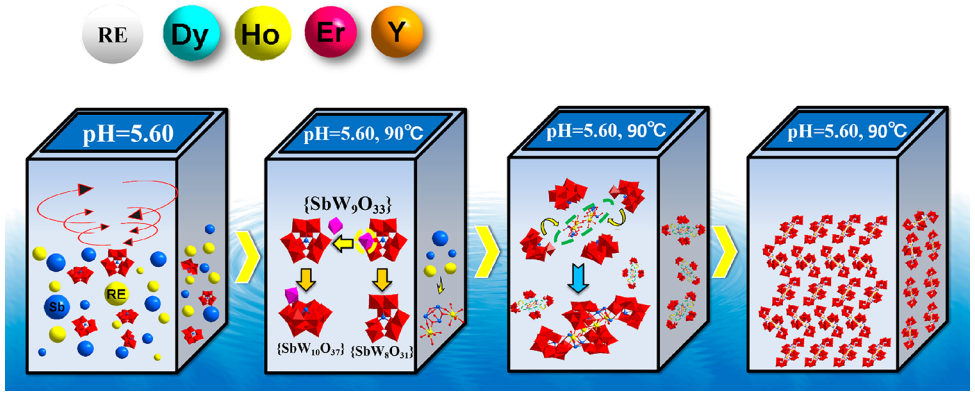

Figure 1. Synthetic procedure for **1**–**4**.

extra Sb^{3+} ions to HPOTs are rare. For example, in 2002, Gouzerh and his collaborators created a Ce^{3+}-containing POM derivative, $[(SbW_9O_{33})_4\{WO_2(H_2O)\}_2$-$Ce_3(H_2O)_8(Sb_4O_4)]^{19-}$, in which Sb^{3+} and Ce^{3+} ions link four $[SbW_9O_{33}]^{9-}$ units.[27] In 2016, Reinoso's group constructed a series of heterometal TM-RE-substituted ATs, $[Sb_7W_{36}O_{133}RE_3TM_2(OAc)(H_2O)_8]^{17-}$ (RE = La^{3+}–Gd^{3+}, TM = Co^{2+}; RE = Ce^{3+}, TM = Ni^{2+}, Zn^{2+}).[28] In 2017, Kong et al. successfully adopted the anionic template strategy to prepare three $\{Sb_4O_4\}$-bridging TM-RE-substituted ATs, $[RE_3(H_2O)_5Ni(H_2O)_3(Sb_4O_4)(SbW_9O_{33})_3(NiW_6O_{24})$-$(WO_2)_3(CH_3COO)]^{17-}$ (RE = La^{3+}, Pr^{3+}, Nd^{3+}).[29]

RE-substituted HPOT materials (RESHPOTMs) have become a research hotspot in recent years. It is the incorporation of RE ions to the HPOT system which can meet some requirements of multifunctional RESHPOTMs: (a) RE ions can tune the combination of some highly negative anionic HPOT segments,[30−33] giving rise to larger clusters with diverse structures; and (b) RE ions own abundant energy levels so that they can give birth to sharp-featured emission peaks and have a long lifetime in the ultraviolet visible (UV–vis) and near-infared (NIR) ranges via *f*–*f* transitions, which can transfer their luminescence functions to RE-SHPOTMs.[34,35] Notably, HPOTs can perform as eminent blue light emissive activators, and some RE ions can play the role of blue light receptors through some *f*–*f* transitions, such as $^7F_0 \rightarrow {}^5D_2$ transition of Eu^{3+} ion, $^6H_{15/2} \rightarrow {}^6I_{15/2}$ transition of Dy^{3+} ion, $^5I_8 \rightarrow {}^5G_6$ transition of Ho^{3+} ion, and $^4I_{15/2} \rightarrow {}^4F_{7/2}$ transition Er^{3+} ion, which constitute energy transfer (ET) processes from HPOT fragments to RE ions.[36−38] In 1998, Yamase et al. put forward that Eu-based ATs under the irradiation of UV light can absorb short-wavelength energy through the photoexcitation of the O→W ligand-to-metal charge-transfer (LMCT) bands so that AT segments transfer energy from O→M LMCT emission ($^1T_{1u} \rightarrow {}^1A_{1g}$) to *f*–*f* excited energy levels of Eu^{3+} ions.[39] In 2011, Boskovic and co-workers reported the sensitization of organic and inorganic POM ligands to Eu^{3+} and Tb^{3+} ions.[40] In 2016–2018, our group made use of time-resolved emission spectrum (TRES) to probe the ET from O→M LMCT triplet emission of HPOT units to RE ions.[36,41] In 2017–2018, Niu et al. also explored the sensitization of HPOT fragments to Dy^{3+} and Er^{3+} ions.[37] Some examples illustrated that, under the O→M LMCT excitation, the energy migration from HPOT donors to RE receptors can lead to the enhancement of photoluminescence (PL) emission and lifetime of RE ions. At present, only a few examples involving ET processes within RESHPOTMs have been reported; however, a good deal of work involving ET mechanism and detailed PL behaviors resulting from ET process needs to be done.

Under this background, we will study in depth the intramolecular ET process within RESHPOTMs. In the work described in this Article, we successfully constructed a series of tetrameric RE and Sb-oxo-clusters simultaneously connecting to ATs, $[H_2N(CH_3)_2]_8Na_6H_8\{[RE_4(H_2O)_6Sb_6O_4]$-$(SbW_{10}O_{37})_2(SbW_8O_{31})_2\}\cdot 24H_2O$ [RE = Dy^{3+} (**1**), Er^{3+} (**2**), Y^{3+} (**3**), Ho^{3+} (**4**)], by reaction of $Na_9[B\text{-}\alpha\text{-}SbW_9O_{33}]\cdot 19.5H_2O$, dimethylamine hydrochloride (DMA·HCl), $SbCl_3$, and $RE(NO_3)_3\cdot 6H_2O$ in acidic aqueous solution (Figure 1). Their tetrameric polyoxoanions are all constructed from two $[B\text{-}\alpha\text{-}SbW_{10}O_{37}]^{11-}$ and two $[B\text{-}\alpha\text{-}SbW_8O_{31}]^{11-}$ segments encapsulating a RE, and an Sb heterometal $[RE_4(H_2O)_6$-$Sb_6O_4]^{22+}$ cluster. During the course of the reaction, an organic solubilizer (here, DMA·HCl) was introduced to the reaction system to improve the reactivity of $[B\text{-}\alpha\text{-}SbW_9O_{33}]^{9-}$ precursors and RE ions, which can effectively decrease the possibility of precipitate resulting from the rapid combination of $[B\text{-}\alpha\text{-}SbW_9O_{33}]^{9-}$ precursors with RE ions.[42] In this work, we investigate the different degrees of sensitization from AT segments to different *f*–*f* emission bands of RE ions by comparing emission intensities and lifetimes under O→W LMCT excitation of AT segments and *f*–*f* excited transitions of RE ions. Under the excitation at 268 nm derived from the O→W LMCT of AT segments, Dy^{3+} ions in **1** and Er^{3+} ions in **2** absorb the emission energy from AT segments, whereupon the emission intensities were increased and lifetimes were prolonged. Experimental results indicate that Dy^{3+} ions acquire more energy from AT segments in **1** in contrast to Er^{3+} ions in **2**. Moreover, the energy from O→W LMCT emission to the $^4F_{9/2} \rightarrow {}^6H_{15/2}$ transition is the most in comparison with the $^4F_{9/2} \rightarrow {}^6H_{13/2}$ and $^4F_{9/2} \rightarrow {}^6H_{11/2}$ transitions in **1**, and that to the $^2H_{11/2} \rightarrow {}^4I_{15/2}$ transition is more than the $^4S_{3/2} \rightarrow {}^4I_{15/2}$ transition in **2**. Energy level diagrams for **1** and **2** are provided. The CIE chromaticity coordinates, color purities, and correlated color temperatures of **1** and **2** are also calculated.

RESULTS AND DISCUSSION

Structural Description. Crystallographic data of **1**–**4** are listed in Table S1. The phase purity of **1**–**4** was determined by comparing the experimental PXRD patterns with the simulated XRD patterns from single-crystal structure analysis of the

DOI: 10.1021/acs.inorgchem.9b01570
Inorg. Chem. 2019, 58, 11636–11648

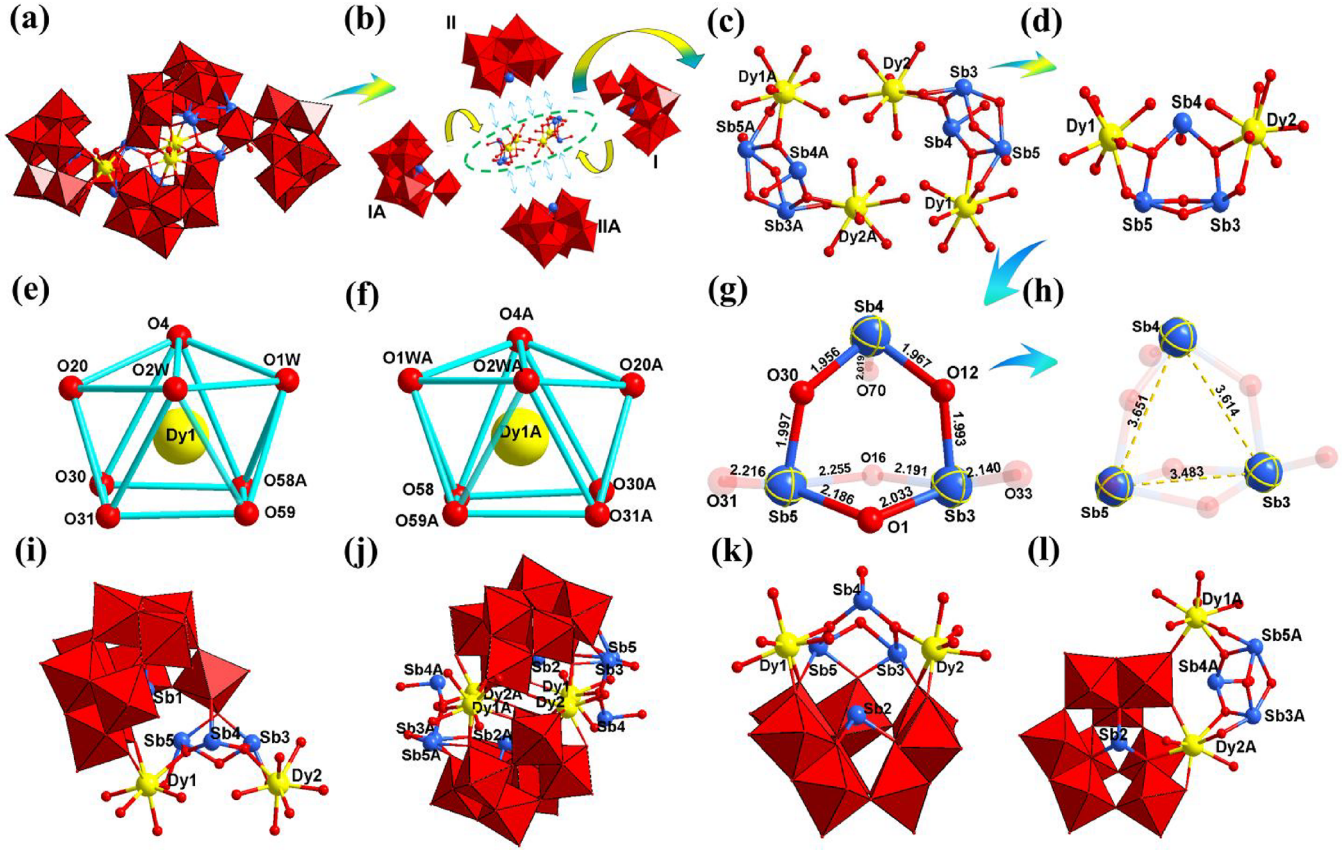

Figure 2. (a) Centrosymmetric tetrameric polyoxoanion $\{[Dy_4(H_2O)_6Sb_6O_4](SbW_{10}O_{37})_2(SbW_8O_{31})_2\}^{22-}$ in **1**. (b) Schematic view of the polyoxoanion in **1**. (c) View of the $\{Dy_4Sb_6\}$ cluster consisting of two $\{Dy_2Sb_3\}$ groups. (d) View of the $\{Dy_2Sb_3\}$ group. (e) Distorted square antiprismatic geometry of the $Dy1^{3+}$ ion. (f) Distorted square antiprismatic geometry of the $Dy2^{3+}$ ion. (g) Twisted hexagon formed by $Sb3^{3+}$, $Sb4^{3+}$, and $Sb5^{3+}$ ions together with three bridging μ_2-O-atoms. (h) Triangle geometry formed by $Sb3^{3+}$, $Sb4^{3+}$, and $Sb5^{3+}$ ions. (i) Combination of one **I** subunit with one $\{Dy_2Sb_3\}$ group. (j) Combination of **II** and **IIA** subunits with a $\{Dy_4Sb_6\}$ group. (k) Combination of one **II** subunit with one $\{Dy_2Sb_3\}$ group. (l) Combination of one **II** subunit with the other $\{Dy_2Sb_3\}$ group. Symmetry code: A, $-2-x, -y, -2-z$. Code: $\{WO_6\}$, red octahedra; O, rose red spheres; W, green spheres; Sb, cyanine spheres; Dy, bright yellow spheres.

samples (Figure S1). **1**−**4** are isomorphic and belong to the monoclinic space group $P2(1)/n$. The calculation results of bond valence sum (BVS) demonstrate that the oxidation states of the W, Sb, and RE centers in the polyoxoanions of **1**−**4** are +6, +3, and +3, respectively (Table S2). The molecular units of **1**−**4** consist of one tetrameric $\{[RE_4(H_2O)_6Sb_6O_4](SbW_{10}O_{37})_2(SbW_8O_{31})_2\}^{22-}$ polyoxoanion, eight monoprotonated $[H_2N(CH_3)_2]^+$ cations, six Na^+ cations, eight protons, and 24 lattice water molecules. In this paper, **1** is selected to exemplify the structural description. The centrosymmetric tetrameric polyoxoanion $\{[Dy_4(H_2O)_6Sb_6O_4](SbW_{10}O_{37})_2(SbW_8O_{31})_2\}^{22-}$ (Figure 2a) in **1** is constituted by two $[SbW_{10}O_{37}]^{11-}$ (**I** and **IA**) subunits and two [B-α-$SbW_8O_{31}]^{11-}$ (**II** and **IIA**) subunits capturing a RE and Sb heterometal $[RE_4(H_2O)_6Sb_6O_4]^{22+}$ cluster through 28 μ_2-O-atoms (Figure 2b). Four Sb^{3+} heteroatoms (i.e., Sb1, Sb1A, Sb2, and Sb2A) in **I**, **IA**, **II**, and **IIA** show a parallelogram distribution and are located on four vertexes of the parallelogram. The distances of Sb1···Sb2 and Sb1···Sb2A are 7.759 and 10.043 Å, respectively (Figure S2a). The Dy^{3+} and Sb^{3+} heterometal $[Dy_4(H_2O)_6Sb_6O_4]^{22+}$ ($\{Dy_4Sb_6\}$) cluster can be regarded as a fusion of two same $[Dy_2(H_2O)_3Sb_3O_2]^{11+}$ ($\{Dy_2Sb_3\}$) groups connected by **I**, **IA**, **II**, and **IIA** (Figure 2b,c). Each $\{Dy_2Sb_3\}$ group is composed of one $[Dy1(H_2O)_2]^{3+}$ ion, one $[Dy2(H_2O)]^{3+}$ ion and one $[Sb_3O_2]^{5+}$ segment (Figure 2d). Four Dy^{3+} centers in two $\{Dy_2Sb_3\}$ groups are aligned in the parallelogram mode, and the distances of Dy1···Dy2 and Dy1···Dy2A are 5.969 and 6.476 Å, respectively (Figure S2b). In the $\{Dy_2Sb_3\}$ group, although two crystallographically independent Dy^{3+} ions ($Dy1^{3+}$, $Dy2^{3+}$) exhibit the octa-coordinate distorted square antiprismatic geometries (Figure 2e,f, Figure S3), their coordination environments are somewhat different. Specifically, the square antiprism of the $Dy1^{3+}$ ion is defined by two μ_2-O-atoms from two $\{WO_6\}$ octahedra of **I** [Dy1−O4, 2.320(9) Å; Dy1−O20, 2.407(10) Å], two μ_2-O-atoms from **II** [Dy1−O31, 2.357(9) Å; Dy1−O59, 2.285(9) Å], and one μ_2-O-atom from **IIA** [Dy1−O58A, 2.308(9) Å], one μ_2-O-atom that combines $Sb4^{3+}$ with $Sb5^{3+}$ ions [Dy1−O30, 2.484(9) Å], and two water ligands [Dy1−O1W, 2.416(11) Å; Dy1−O2W, 2.380(10) Å]. In contrast, the square antiprism of the $Dy2^{3+}$ ion is constructed from four μ_2-O-atoms from three $\{WO_6\}$ octahedra of **IIA** [Dy2−O45A, 2.319(9) Å; Dy2−O60A, 2.632(9) Å; Dy2−O61A, 2.283(9) Å; Dy2−O68A, 2.279(9) Å], two μ_2-O-atoms from **II** [Dy2−O17, 2.309(9) Å; Dy2−O33, 2.436(9) Å], one μ_2-O-atom that combines $Sb3^{3+}$ with $Sb4^{3+}$ ions [Dy2−O12, 2.480(9) Å], and one coordinate water molecule [Dy2−O3W, 2.455(10) Å]. In each $[Sb_3O_2]^{5+}$ group, three Sb^{3+} centers (i.e., $Sb3^{3+}$, $Sb4^{3+}$, and $Sb5^{3+}$) connect to each other by two μ_2-O-atoms (O30, O12) sharing with $Dy1^{3+}$ and $Dy2^{3+}$ ions and two μ_2-O-atoms (O1, O16) from **I** and **II**, resulting in the formation of a tri-Sb^{3+} ring. The $Sb3^{3+}$, $Sb4^{3+}$,

DOI: 10.1021/acs.inorgchem.9b01570
Inorg. Chem. 2019, 58, 11636−11648

and $Sb5^{3+}$ ions together with three bridging μ_2-O-atoms can be treated as a twisted hexagon, in which the three-Sb^{3+} center enjoys different coordination modes (Figure 2g, Figure S4a,b). Specifically, the $Sb3^{3+}$ and $Sb5^{3+}$ centers show the tetra-coordinate tetragonal pyramidal geometry [Sb−O, 1.994(9)−2.252(10) Å], while the $Sb4^{3+}$ ion exhibits the tri-coordinate trigonal pyramidal geometry [Sb−O, 1.957(9)−2.022(9) Å] (Figure S5a−f). It is of interest that, if these four μ_2-O-atoms of the tri-Sb^{3+} ring are removed, they show a triangle geometry (Figure 2h, Figure S4c,d). On one hand, the $[SbW_{10}O_{37}]^{11-}$ subunit (**I**) can be viewed as a trivacant $[B\text{-}\alpha\text{-}SbW_9O_{33}]^{9-}$ subunit grafted by an additional $\{WO_6\}$ octahedron (Figure S6a), which offers four μ_2-O-atoms to coordinate to one adjacent $\{Dy_2Sb_3\}$ group (Figure 2i). On the other hand, **II** and **IIA** are connected with each other by a $\{Dy_4Sb_6\}$ group (Figure 2j), in which the $[B\text{-}\alpha\text{-}SbW_8O_{31}]^{11-}$ subunit (**II**) can be considered as a trivacant $[B\text{-}\alpha\text{-}SbW_9O_{33}]^{9-}$ subunit that lost one $\{WO_6\}$ octahedron in the vacancy position (Figure S6b), which bonds to one $\{Dy_2Sb_3\}$ group through five μ_2-O-atoms (Figure 2k) and connects to the other $\{Dy_2Sb_3\}$ group by five μ_2-O-atoms (Figure 2l). Therefore, two separated $\{Dy_2Sb_3\}$ groups packaged by **I**, **IA**, **II**, and **IIA** play an important role in forming the structure construction and maintaining the stability of the structure.

In addition, the 4×4×4 supramolecular 3-D stacking representations of **1** and the simplified representations viewed along *a* and *c* axis illustrate that the tetrameric polyoxoanions of **1** are regularly arranged in the mode of −ABAB− (Figure 3). Along the *c* direction, neighboring tetrameric polyoxoanions are parallel to each other; however, along the *b* direction, neighboring tetrameric polyoxoanions are oppositely aligned in a staggered fashion (Figure 3a). Intriguingly, neighboring tetrameric polyoxoanions along the *b* direction shows the wave-like distribution (Figure 3b, Figure S7). The wave-like arrangement of tetrameric polyoxoanions can effectively enhance the space utilization and adopt the closest packing fashion. Viewed along the *c* axis, the dihedral angle formed by two neighboring tetrameric polyoxoanions is smaller than that viewed along the *a* axis (Figure 3b,c). It is obvious that Na^+ ions, monoprotonated $[H_2N(CH_3)_2]^+$ cations, and lattice water molecules are wrapped in the interspace surrounded by tetrameric polyoxoanions. The N-atoms on $[H_2N(CH_3)_2]^+$ cations interact with the surface O-atoms of tetrameric polyoxoanions and water molecules by hydrogen-bonding interactions with N−H···O distances of 2.93(2)−3.10(2) Å (Figure S8).

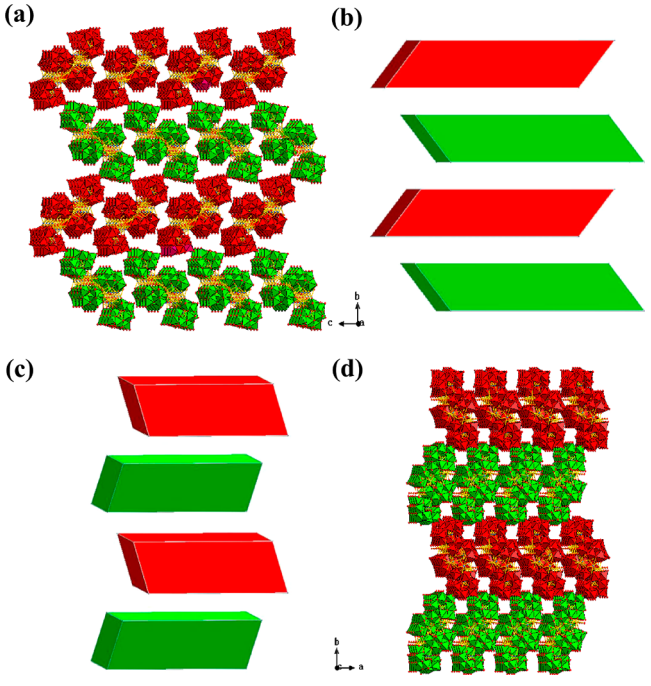

Figure 3. (a) The 4×4×4 supramolecular 3-D stacking of **1** viewed along the *a* axis. (b) Simplified scheme of the supramolecular 3-D stacking of **1** viewed along the *a* axis. (c) The 4×4×4 supramolecular 3-D stacking of **1** viewed along the *c* axis. (d) Simplified scheme of the supramolecular 3-D stacking of **1** viewed along the *c* axis. Na^+ ions, $[H_2N(CH_3)_2]^+$ cations, and lattice water molecules are omitted for clarity.

If **1** is imagined as a sandwich-type cluster $\{[Dy_4(H_2O)_6Sb_6O_4](SbW_8O_{31})_2\}$ carrying two $[SbW_{10}O_{37}]^{11-}$ subunits on both sides (Figure 4a), it is completely different from those previously reported Krebs-type sandwich-type ATs.[37−39] In 2009 and 2012, Kortz's group discovered two Krebs-type sandwich-type Ru-encapsulated ATs $[Sb_2W_{20}O_{70}(Ru^{II}C_6H_6)_2]^{10-}$ (**5**) (Figure 4b) and $[\{Ru^{IV}_4O_6(H_2O)_9\}_2Sb_2W_{20}O_{68}(OH)_2]^{4-}$ (**6**) (Figure 4c).[43,44] In 2013, Hill et al. addressed a Krebs-type sandwich-type carbonyl metal-substituted AT $[Sb_2W_{20}O_{70}\{Re^{I}(CO)_3\}_2]^{12-}$ (**7**) (Figure 4c).[45] Obviously, the sandwich-type AT cluster core carries two organoruthenium $[Ru^{II}C_6H_6]^{2+}$ groups for **5**, two cubane-like tetra-Ru $[Ru^{IV}_4O_6(H_2O)_9]^{4+}$ groups for **6** and two tricarbonyl rhenium $[Re(CO)_3]^{4+}$ groups for **7** on both sides; however, in **1**, the Dy^{III}-/Sb^{III}-oxo-cluster bridging AT cluster core $\{[Dy_4(H_2O)_6Sb_6O_4](SbW_8O_{31})_2\}$ is supported by two $[B\text{-}\alpha\text{-}SbW_{10}O_{37}]^{11-}$ subunits on both sides. If **1** is considered as a tetrameric AT cluster that consists of by two $[B\text{-}\alpha\text{-}SbW_{10}O_{37}]^{11-}$ and two $[B\text{-}\alpha\text{-}SbW_8O_{31}]^{11-}$ subunits (Figure 4e), in which four Sb^{III}-atoms in two $[B\text{-}\alpha\text{-}SbW_{10}O_{37}]^{11-}$ and two $[B\text{-}\alpha\text{-}SbW_8O_{31}]^{11-}$ subunits utilize the parallelogram alignment, it is distinct from those previously reported tetrameric TM-substituted polyoxotungstates including four lacunary POM subunits.[46−49] In 2014, Gutiérrez-Zorrilla and partners obtained a 2,3-pyzdc-bridging Ni^{II}-substituted tetrameric AT $[(2,3\text{-pyzdc})_2\{NaNi_2(H_2O)_4Sb_2W_{20}O_{70}\}_2]^{22-}$ (**8**) containing four $[B\text{-}\beta\text{-}SbW_9O_{33}]^{9-}$ subunits (2,3-pyzdc = pyrazine-2,3-dicarboxylic acid), in which four Sb^{III} heteroatoms show a twisted parallelogram geometry (Figure 4f).[46] In the same year, Su and collaborators reported a tetrameric Zr^{IV}-substituted selenotungstate $[(\alpha\text{-}SeW_9O_{34})\{Zr(H_2O)\}\{WO(H_2O)\}(WO_2)(SeO_3)\{\alpha\text{-}SeW_8O_{31}Zr(H_2O)\}]_2^{12-}$ (**9**) comprising two $[\alpha\text{-}SeW_9O_{34}]^{10-}$ and two $[\alpha\text{-}SeW_8O_{31}]^{10-}$ subunits, in which four Se^{IV} heteroatoms in $[\alpha\text{-}SeW_9O_{34}]^{10-}$ and $[\alpha\text{-}SeW_8O_{31}]^{10-}$ subunits exhibit a parallelogram distribution (Figure 4g).[47] In 2016, Kortz's group obtained a mixed-valence Mn-substituted tetrahedral cluster $[Mn^{III}_{10}Mn^{II}_6O_6(OH)_6(PO_4)_4(A\text{-}\alpha\text{-}SiW_9O_{34})_4]^{28-}$ (**10**) anchoring four $[A\text{-}\alpha\text{-}SiW_9O_{34}]^{10-}$ subunits, in which four Si^{IV}-atoms present a regular tetrahedral geometry (Figure 4h).[48] In 2018, Yang and cooperators published a tetrameric Zr^{IV}-containing polyoxotungstate $[Zr_4(\beta\text{-}GeW_{10}O_{38})_2(A\text{-}\beta\text{-}PW_9O_{34})_2]^{26-}$ (**11**) incorporating two $[\beta\text{-}GeW_{10}O_{38}]^{12-}$ and two $[A\text{-}\beta\text{-}PW_9O_{34}]^{6-}$ subunits, in which two Ge^{IV} and two P^{V} heteroatoms are arranged in an irregular quadrilateral motif (Figure 4i).[49]

Photoluminescence (PL) Properties. Because a matter is selective in the absorption of light, different incident lights

DOI: 10.1021/acs.inorgchem.9b01570
Inorg. Chem. 2019, 58, 11636−11648

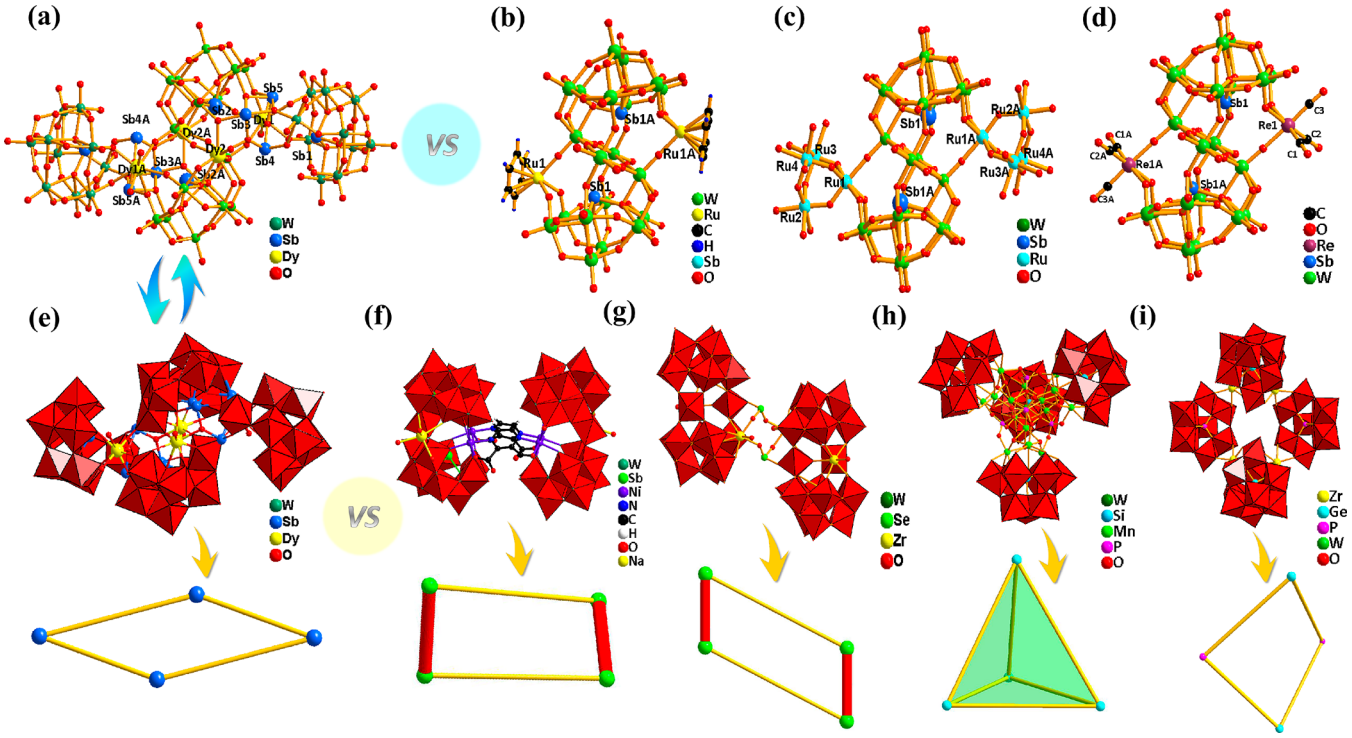

Figure 4. (a–d) Ball-and-stick views of **1** (a), **5** (b), **6** (c), and **7** (d). (e–i) Combined polyhedral and ball-and-stick views of **1** (e), **8** (f), **9** (g), **10** (h), and **11** (i).

have different excitation efficiency. According to previous reports, under the irradiation of ultraviolet light, RESHPOTMs not only can emit a broad $^3T_{1u}\rightarrow{}^1A_{1g}$ emission band from the O→W LMCT triplet states of HPOT fragments, but also can also show the *f*–*f* emission bands of RE ions.[36,37] Moreover, transfer energy from HPOT fragments to RE ions via radiation reabsorption and non-radiative relaxation has been observed.[36,37] However, different excitation lights will lead to the different emission intensities, therefore, the selection of the appropriate excitation wavelength and the influence of the different excitation wavelengths on the emission intensities become very important in the study of luminescent materials. In the Article, to probe the appropriate excitation wavelengths and the influence of the different excitation wavelengths on the emission intensities of **1** and **2**, the PL properties of solid samples of **1** and **2** are systemically investigated upon excitations of the O→W LMCT transition of AT segments and the strongest *f*–*f* transition of RE ions at room temperature. The occurrence of intramolecular ET process from AT segments to RE ions in **1** and **2** can be proved by two observations: (i) the $^3T_{1u}\rightarrow{}^1A_{1g}$ emission band of AT fragments overlaps with the excitation peaks of RE ions;[50−53] (ii) the PL emission intensity of RE ions will be enhanced and the PL lifetimes of RE ions will be prolonged upon the O→W LMCT excitation of AT segments in comparison with those under the strongest *f*–*f* excitation of RE ions.[54,55] Their energy level diagrams are also given to elucidate the ET process from AT segments to RE ions in **1** and **2**. In addition, under the O→W LMCT excitation, the emission spectrum, excitation spectrum, and time-resolved emission spectrum (TRES) of **3** are also measured (Figure S9a–c). Figure S9a only exhibits the $^3T_{1u}\rightarrow{}^1A_{1g}$ emission band centered at 470 nm because Y^{3+} ions have no PL emission in this region whereas Figure S9b displays the O→W LMCT excitation band centered at 268 nm.

Under the O→W LMCT excitation at 268 nm, the PL emission spectrum of **1** in the range of 300−700 nm shows a broad band varying from 350 to 500 nm with maximum ca. 470 nm ascribed to the $^3T_{1u}\rightarrow{}^1A_{1g}$ transition originating from AT segments (the black line in Figure 5a) and three obvious *f*–*f* emission peaks at 483, 575, and 663 nm respectively attributable to the $^4F_{9/2}\rightarrow{}^6H_{15/2}$, $^4F_{9/2}\rightarrow{}^6H_{13/2}$, and $^4F_{9/2}\rightarrow{}^6H_{11/2}$ transitions of Dy^{3+} ions (the black line in Figure 5b).[56−58] Through monitoring the strongest emission peak at 575 nm of Dy^{3+} ions, the obtained excitation spectrum (250−470 nm) of **1** shows a broad O→W LMCT excitation band (LMCTB) centered at ca. 268 nm derived from AT segments and a series of excitation peaks at 352, 366, 389, 427, and 453 nm ascribed to the $^6H_{15/2}\rightarrow{}^6P_{7/2}$, $^6H_{15/2}\rightarrow{}^6P_{5/2}$, $^6H_{15/2}\rightarrow{}^6I_{13/2}$, $^6H_{15/2}\rightarrow{}^6G_{11/2}$, and $^6H_{15/2}\rightarrow{}^6I_{15/2}$ transitions of Dy^{3+} ions (the red line in Figure 5a).[56] It can be explicitly seen from Figure 5a that the wide emission band (350−500 nm) of AT segments in the emission spectrum of **1** overlaps well with the excitation peaks of Dy^{3+} ions in the excitation spectrum of **1**, indicating the occurrence of intramolecular ET process from AT segments to Dy^{3+} ions. In comparison, the emission spectra of **1** between 470 and 700 nm under the excitations at 268 and 450 nm at room temperature are displayed in Figure 5b. Notably, the excitation wavelength at 450 nm is derived from the excitation spectrum of **1** (Figure S10a). As apparently shown in Figure 5b, the intensities of three emission peaks of Dy^{3+} ions under the O→W LMCT excitation at 268 nm are higher obviously than those under the strongest *f*–*f* excitation at 450 nm of Dy^{3+} ions, which can strongly indicate that the PL emission of Dy^{3+} ions is sensitized by AT segments.

As known to all, the magnetic dipole transition ($^4F_{9/2}\rightarrow{}^6H_{15/2}$) hardly changes with the coordination environment, and crystal field strength of Dy^{3+} ions and the hypersensitive electric dipole transition ($^4F_{9/2}\rightarrow{}^6H_{13/2}$) can be greatly affected

DOI: 10.1021/acs.inorgchem.9b01570
Inorg. Chem. 2019, 58, 11636−11648

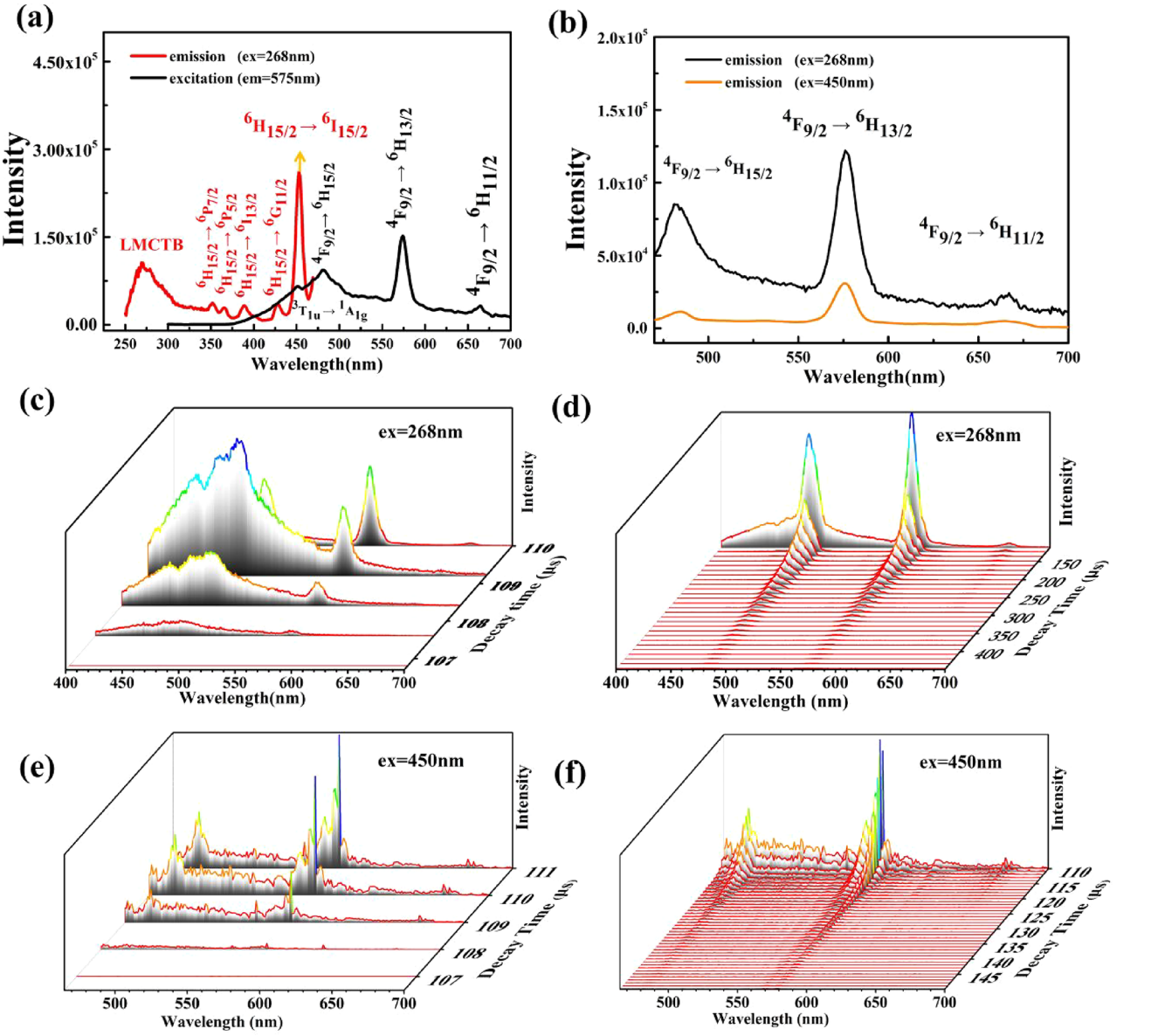

Figure 5. (a) Solid-state emission spectrum of **1** in the range of 300−700 nm under the O→W LMCT excitation at 268 nm, and solid-state excitation spectrum of **1** in the range of 250−470 nm obtained by monitoring the emission ($^4F_{9/2}\rightarrow{}^6H_{13/2}$) at 575 nm of Dy^{3+} ions. (b) Comparison of the solid-state emission spectra of **1** under the excitations at 268 and 450 nm. (c−f) TRES spectra of **1** under excitation at 268 nm (106.8−110.0 μs) (c), under excitation at 268 nm (110.0−450.0 μs) (d), under excitation at 450 nm (107−111.0 μs) (e), and under the excitation at 450 nm (110.0−450.0 μs) (f).

by the chemical environment around Dy^{3+} ions. When Dy^{3+} ions take up low symmetric sites without inversion center, the electric dipole transition ($^4F_{9/2}\rightarrow{}^6H_{15/2}$) is dominant in emission spectrum and its intensity is much higher than that of magnetic dipole transition ($^4F_{9/2}\rightarrow{}^6H_{15/2}$).[57,59] As shown in Figure 5b, the intensity ratio of $I(^4F_{9/2}\rightarrow{}^6H_{15/2})/I(^4F_{9/2}\rightarrow{}^6H_{13/2})/I(^4F_{9/2}\rightarrow{}^6H_{11/2})$ is ca. 5.01:5.09:1.00 upon λ_{ex} = 268 nm and 2.65:5.00:1.00 upon λ_{ex} = 450 nm. The calculated results demonstrate that Dy^{3+} ions occupy lattice site without inversion center, which accord with the structural analysis that Dy^{3+} ions exhibit the octa-coordinate distorted square antiprismatic geometries. The different intensity ratios of $I(^4F_{9/2}\rightarrow{}^6H_{15/2})/I(^4F_{9/2}\rightarrow{}^6H_{13/2})/I(^4F_{9/2}\rightarrow{}^6H_{11/2})$ upon λ_{ex} = 268 nm and λ_{ex} = 450 nm directly indicates that AT segments may play different sensitization roles in the $^4F_{9/2}\rightarrow{}^6H_{15/2}$, $^4F_{9/2}\rightarrow{}^6H_{13/2}$, and $^4F_{9/2}\rightarrow{}^6H_{11/2}$ transitions of Dy^{3+} ions, of which the emission intensity of the $^4F_{9/2}\rightarrow{}^6H_{15/2}$ transition of Dy^{3+} ions is more apparently enhanced than those of the $^4F_{9/2}\rightarrow{}^6H_{13/2}$ and $^4F_{9/2}\rightarrow{}^6H_{11/2}$ transitions after acquiring the sensitization of AT segments. In other words, under the O→W LMCT excitation, the $^4F_{9/2}\rightarrow{}^6I_{15/2}$ emission transition of Dy^{3+} ions may receive the most energy from the $^3T_{1u}\rightarrow{}^1A_{1g}$ LMCT transition of AT segments, closely followed by the $^4F_{9/2}\rightarrow{}^6H_{13/2}$ transition, and the $^4F_{9/2}\rightarrow{}^6H_{11/2}$ transition receives the least energy.

Moreover, to analyze the ET process, TRES spectra of **1** under the excitations at 268 and 450 nm were collected in the range of 400−700 nm. It can be apparently observed from Figure 5c that, upon the excitation at 268 nm, the intensities of the abroad emission band at ca. 470 nm and three emission peaks at 483, 575, and 663 nm start to increase at 106.8 μs, and the intensity of the $^3T_{1u}\rightarrow{}^1A_{1g}$ emission band reaches the

DOI: 10.1021/acs.inorgchem.9b01570
Inorg. Chem. 2019, 58, 11636−11648

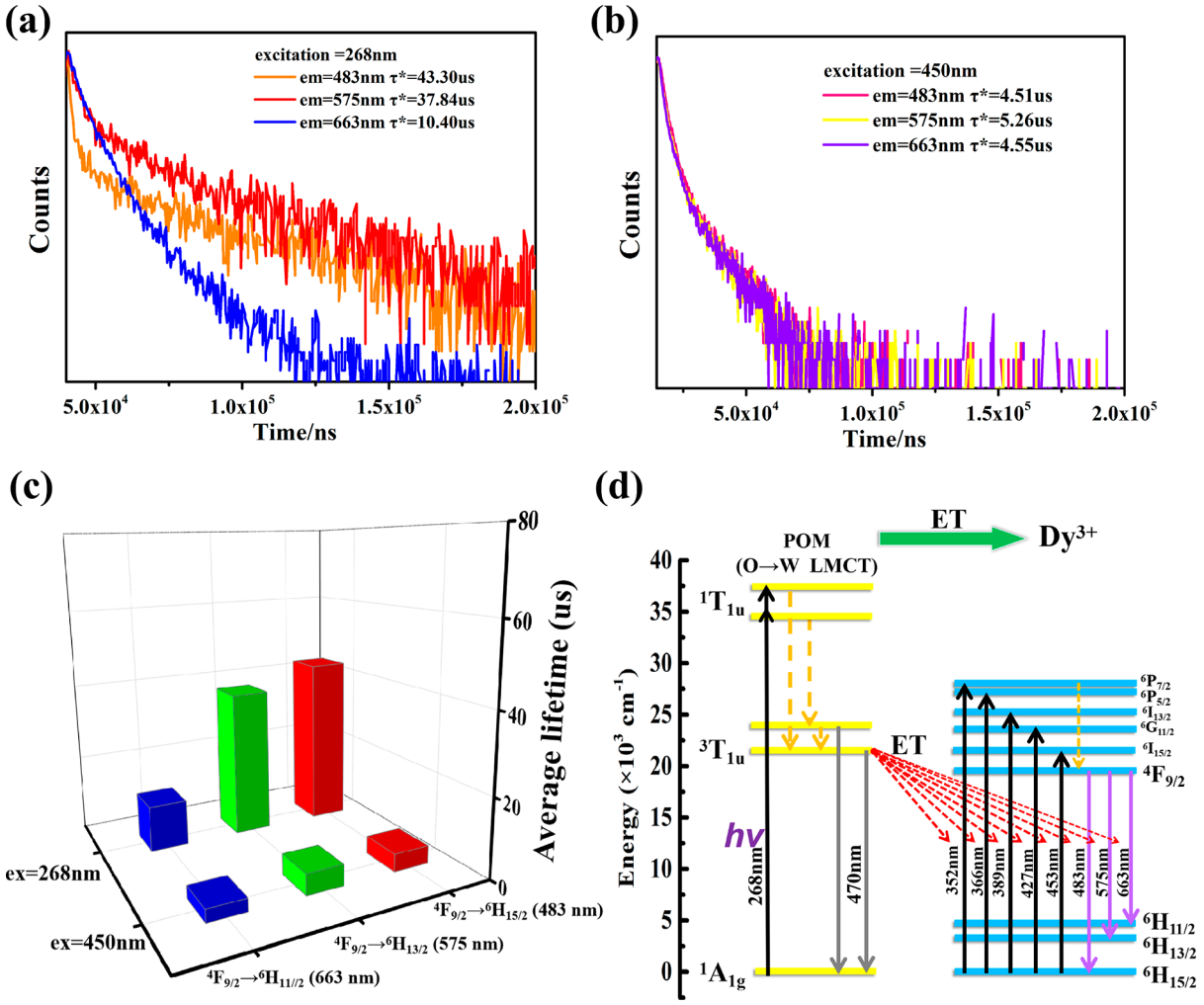

Figure 6. (a) Comparison of the PL decay curves of **1** obtained by monitoring the emission peaks at 483, 575, and 663 nm upon the excitation at 268 nm. (b) Comparison of the PL decay curves of **1** obtained by monitoring the emission peaks at 483, 575, and 663 nm upon the excitation at 450 nm. (c) Comparison of the calculated average lifetimes for the $^4F_{9/2}\rightarrow{}^6H_{15/2}$, $^4F_{9/2}\rightarrow{}^6H_{13/2}$, and $^4F_{9/2}\rightarrow{}^6H_{11/2}$ emission peaks of Dy^{3+} ions upon the excitation at 268 and 450 nm. (d) Schematic energy level diagram of indicating the ET process from AT segments to Dy^{3+} ions. (The solid line is radiation transition, and the dotted line is non-radiative transition.)

maximum at 109.2 μs. Thereafter, the intensity of the $^3T_{1u}\rightarrow{}^1A_{1g}$ emission band begins to weaken; however, the intensities of three *f*–*f* emission peaks further increase, and their intensities reach the most at ca. 110.0 μs, which unambiguously consolidate that ET occurs from AT segments to Dy^{3+} ions. It should be pointed out that the intensity of the $^4F_{9/2}\rightarrow{}^6H_{15/2}$ emission at 109.2 μs is higher than that of the $^4F_{9/2}\rightarrow{}^6H_{13/2}$ emission at 110.0 μs, which implies that $^4F_{9/2}\rightarrow{}^6H_{15/2}$ emission receives energy from the $^3T_{1u}\rightarrow{}^1A_{1g}$ emission earlier and more than the $^4F_{9/2}\rightarrow{}^6H_{13/2}$ emission. Until 120 μs, the $^3T_{1u}\rightarrow{}^1A_{1g}$ emission band at ca. 470 nm disappears and the intensities of three emission peaks at 483, 575, and 663 nm continue to decline, indicating that the ET process from AT segments to Dy^{3+} ions has been accomplished (Figure 5d). Finally, at 162 μs, the emission peak at 663 nm disappears, but the peaks at 483 and 575 nm disappear at 435 and 383 μs, which demonstrates that the decay rate of the $^4F_{9/2}\rightarrow{}^6H_{15/2}$ emission is the slowest, closely followed by the $^4F_{9/2}\rightarrow{}^6H_{13/2}$ emission, and the decay rate of the $^4F_{9/2}\rightarrow{}^6H_{11/2}$ emission is the fastest. Moreover, upon the excitation at 450 nm, TRES of **1** was also collected, and three *f*–*f* emission peaks start at 107 μs and reach maximum at ca. 110 μs (Figure 5e). As time goes on, the strong peaks at 481 and 577 nm disappear at 142 and 146 μs, and the weak peak at 669 nm disappears at 119 μs (Figure 5f). From 107 to 146 μs, the intensity of $^4F_{9/2}\rightarrow{}^6H_{13/2}$ emission is the highest, the $^4F_{9/2}\rightarrow{}^6H_{15/2}$ emission is second, and the $^4F_{9/2}\rightarrow{}^6H_{11/2}$ emission is the weakest. These observations also suggest that the decay rate of $^4F_{9/2}\rightarrow{}^6H_{13/2}$ emission is the slowest, closely followed by the $^4F_{9/2}\rightarrow{}^6H_{15/2}$ emission, and the $^4F_{9/2}\rightarrow{}^6H_{11/2}$ emission is the fastest. Comparison of the decay rates of three *f*–*f* emission peaks upon the excitations at 268 and 450 nm reveals that the decay behaviors of three *f*–*f* emission peaks are in some degree inhibited upon the excitation at 268 nm, mainly because the sensitization of AT segments to the $^4F_{9/2}\rightarrow{}^6H_{15/2}$ emission of Dy^{3+} ions is larger than those of the $^4F_{9/2}\rightarrow{}^6H_{13/2}$ emission and only little sensitization toward the $^4F_{9/2}\rightarrow{}^6H_{11/2}$ emission of Dy^{3+} ions. Thus, it can be summarized that under the O→W LMCT excitation the most energy migrates from AT segments to the $^4F_{9/2}\rightarrow{}^6H_{15/2}$ emission and followed by the $^4F_{9/2}\rightarrow{}^6H_{13/2}$ emission, only little energy migrates to the $^4F_{9/2}\rightarrow{}^6H_{11/2}$ emission of Dy^{3+} ions.

DOI: 10.1021/acs.inorgchem.9b01570
Inorg. Chem. 2019, 58, 11636−11648

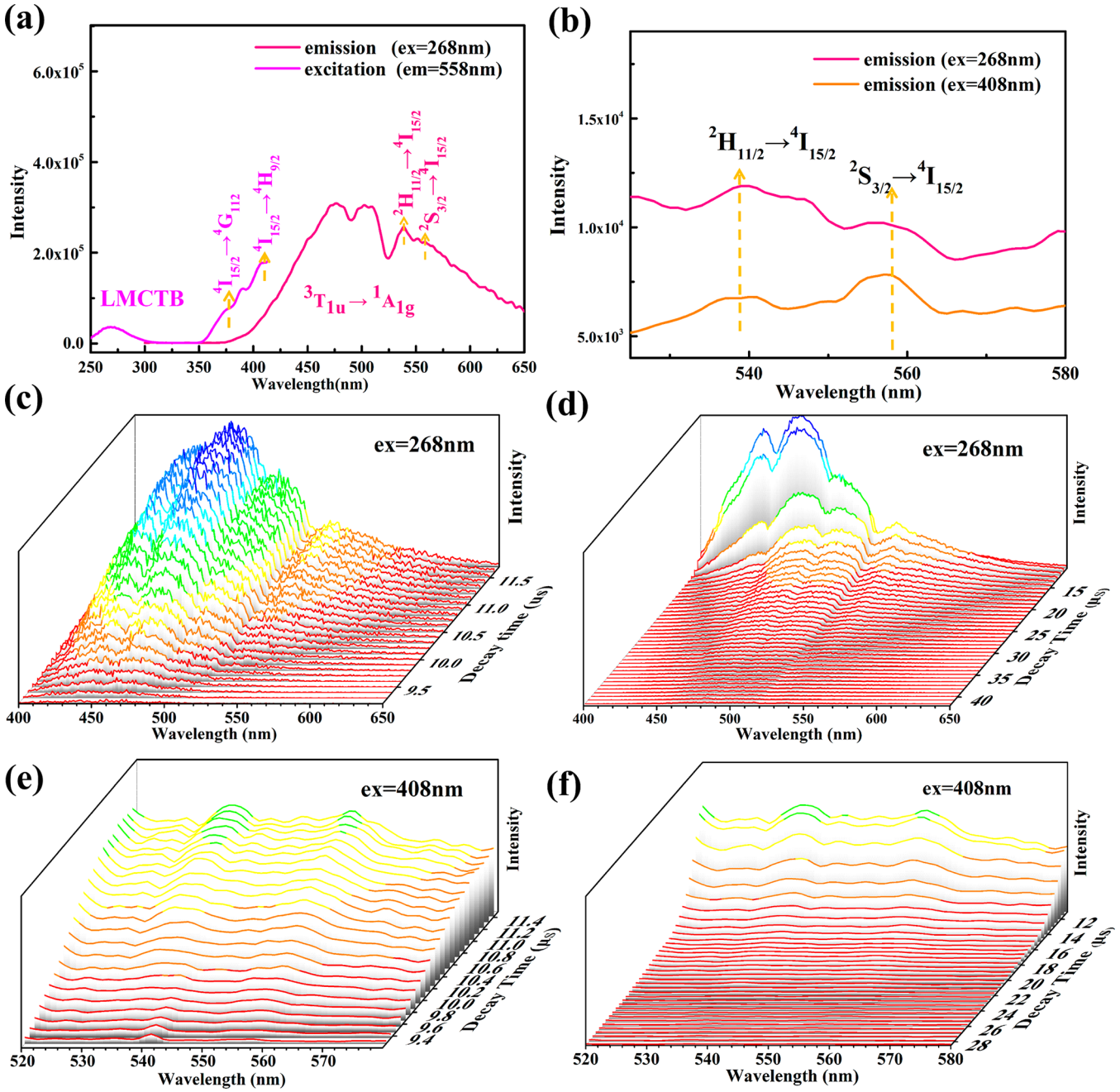

Figure 7. (a) Solid-state emission spectrum of **2** in the range of 300−700 nm under the O→W LMCT excitation at 268 nm and the excitation spectrum of **2** in the range of 250−410 nm obtained under monitoring the emission ($^4S_{3/2}\rightarrow{}^4I_{15/2}$) at 558 nm. (b) Solid-state emission spectra of **2** under excitation at 268 and 408 nm. (c) TRES spectra of **2** (the decay time range is 9.2−11.7 μs) under the excitation at 268 nm. (d) TRES spectra of **2** (the decay time range is 11.4−39.9 μs) under the excitation at 268 nm. (e) TRES spectra of **2** (the decay time range is 9.1−11.5 μs) under the excitation at 408 nm. (f)TRES spectra of **2** (the decay time range is 11.4−28.5 μs) under the excitation at 408 nm.

To compare the ET efficiency from the $^3T_{1u}\rightarrow{}^1A_{1g}$ emission to $^4F_{9/2}\rightarrow{}^6H_{15/2}$, $^4F_{9/2}\rightarrow{}^6H_{13/2}$, and $^4F_{9/2}\rightarrow{}^6H_{11/2}$ emissions of Dy^{3+} ions in **1**, we can make the conclusion by monitoring different emission peaks of Dy^{3+} ions through testing PL lifetimes under O→W LMCT excitation at 268 nm and the strongest *f*–*f* excitation at 450 nm of Dy^{3+} ions. All the decay lifetime curves can be fitted with the second-order exponential function 1:[42]

$$I = A_1 \exp(-t/\tau_1) + A_2 \exp(-t/\tau_2) \quad (1)$$

In this equation, t is the decay lifetime, τ_1 and τ_2 are respectively fast and slow components of lifetimes, and A_1 and A_2 are the pre-exponential factors.

The average lifetime (τ^*) can be calculated through eq 2:[60−62]

$$\tau^* = (A_1\tau_1^2 + A_2\tau_2^2)/(A_1\tau_1 + A_2\tau_2) \quad (2)$$

Sensitization of AT segments prolongs the PL lifetime of *f*–*f* emissions of Dy^{3+} ions. As shown in Figures 6a,b and Table S4, the PL decay lifetime curves of the $^4F_{9/2}\rightarrow{}^6H_{15/2}$, $^4F_{9/2}\rightarrow{}^6H_{13/2}$, and $^4F_{9/2}\rightarrow{}^6H_{11/2}$ emission peaks were measured

DOI: 10.1021/acs.inorgchem.9b01570
Inorg. Chem. 2019, 58, 11636−11648

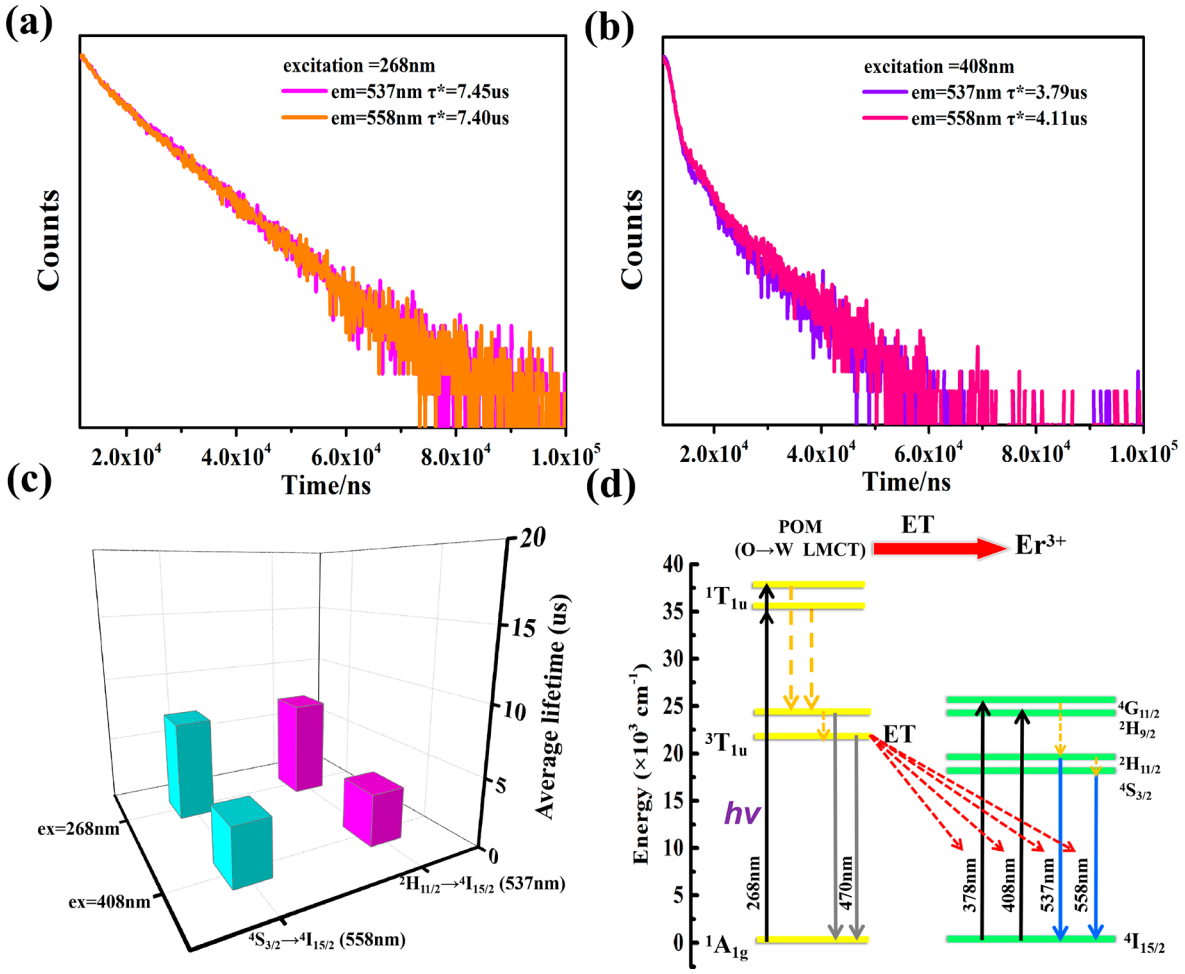

Figure 8. (a) PL lifetime decay curves of **2** by monitoring the peaks at 537 and 558 nm and under excitation at 268 nm. (b) PL lifetime decay curves of **2** by monitoring the peak at 537 and 558 nm and under excitation at 408 nm. (c) Comparison of the calculated average lifetimes for the $^2H_{11/2}\rightarrow{}^4I_{15/2}$ and $^4S_{3/2}\rightarrow{}^4I_{15/2}$ emission peaks of Er^{3+} ions upon the excitation at 268 and 408 nm. (d) Schematic energy level diagram of **2** indicating the ET process from AT fragments to Er^{3+} ions. (The solid line is radiation transition, and the dotted line is non-radiative transition.)

respectively upon the excitations at 268 and 450 nm under the same conditions. Under the excitation at 268 nm, the τ^* values are respectively calculated as 43.30, 37.84, and 10.40 μs for the $^4F_{9/2}\rightarrow{}^6H_{15/2}$, $^4F_{9/2}\rightarrow{}^6H_{13/2}$, and $^4F_{9/2}\rightarrow{}^6H_{11/2}$ emissions (Figure 6a). Under the excitation at 450 nm, the τ^* values are 4.51, 5.26, and 4.55 μs for $^4F_{9/2}\rightarrow{}^6H_{15/2}$, $^4F_{9/2}\rightarrow{}^6H_{13/2}$, and $^4F_{9/2}\rightarrow{}^6H_{11/2}$ emissions (Figure 6b), respectively. The lifetime ratio of $\tau^*(^4F_{9/2}\rightarrow{}^6H_{15/2})/\tau^*(^4F_{9/2}\rightarrow{}^6H_{13/2})/\tau^*(^4F_{9/2}\rightarrow{}^6H_{11/2})$ is ca. 4.16:3.64:1.00 upon the excitation at 268 nm and 0.99:1.16:1.00 upon the excitation at 450 nm (Figure 6c). The lifetimes of three *f*–*f* emissions upon the excitation at 268 nm are all prolonged relative to those upon the excitation at 450 nm, and the lifetimes of $^4F_{9/2}\rightarrow{}^6H_{15/2}$, $^4F_{9/2}\rightarrow{}^6H_{13/2}$, and $^4F_{9/2}\rightarrow{}^6H_{11/2}$ emissions increase by 9.6, 7.19, and 3.29 times. These results illustrate that the sensitization degree of the $^3T_{1u}\rightarrow{}^1A_{1g}$ emission to the $^4F_{9/2}\rightarrow{}^6H_{15/2}$ emission is the highest, the $^4F_{9/2}\rightarrow{}^6H_{13/2}$ emission is the second, and the $^4F_{9/2}\rightarrow{}^6H_{11/2}$ emission is the weakest. The calculated $^3T_{1u}\rightarrow{}^1A_{1g}$ (21.277×10^3 cm^{-1}) energy gap is close to $^4F_{9/2}\rightarrow{}^6H_{15/2}$ (20.704×10^3 cm^{-1}) energy gap (Table S6),[37,63] which implies that the good energy level match will lead to the high sensitization effect.

Based on the above-mentioned analysis, the schematic ET process in **1** is depicted in Figure 6d. During the O→W LMCT excitation, the electrons at the $^1A_{1g}$ ground state jump to the $^1T_{1u}$ excited state by absorbing energy and declined to the $^3T_{1u}$ state through the non-radiative relaxation. When the electrons are back to the ground state in the form of blue emission, part energy from the $^3T_{1u}\rightarrow{}^1A_{1g}$ transition of AT segments is reabsorbed by the $^6H_{15/2}\rightarrow{}^6P_{7/2}$, $^6H_{15/2}\rightarrow{}^6P_{5/2}$, $^6H_{15/2}\rightarrow{}^6I_{13/2}$, $^6H_{15/2}\rightarrow{}^6G_{11/2}$, and $^6H_{15/2}\rightarrow{}^6I_{15/2}$ excited transitions of Dy^{3+} ions and then prompt the $^4F_{9/2}\rightarrow{}^6H_{15/2}$, $^4F_{9/2}\rightarrow{}^6H_{13/2}$, and $^4F_{9/2}\rightarrow{}^6H_{11/2}$ emission transitions.[58] Totally, the AT segments can help to enhance the intensities and prolong the decay lifetimes of three *f*–*f* $^4F_{9/2}\rightarrow{}^6H_{15/2}$, $^4F_{9/2}\rightarrow{}^6H_{13/2}$, and $^4F_{9/2}\rightarrow{}^6H_{11/2}$ emissions of Dy^{3+} ions because of the existence of energy migration from the $^3T_{1u}\rightarrow{}^1A_{1g}$ transition of AT segments to Dy^{3+} ions. Therefore, the O→W LMCT excitation at 268 nm is suitable for **1**.

In **2**, the ET process from AT segments to Er^{3+} ions is similar to that of AT segments to Dy^{3+} ions in **1**. When **2** was excited by the O→W LMCT excitation at 268 nm [The excitation at 268 nm is from the excitation spectrum of **2** (Figure 7a)], its emission spectrum in the range of 300–650 nm reveals a wide emission band (ca. 350–500 nm) at ca. 470 nm ascribed to the $^3T_{1u}\rightarrow{}^1A_{1g}$ transition of AT segments and two emission peaks at 537 and 558 nm assigned to the $^2H_{11/2}\rightarrow{}^4I_{15/2}$ and $^4S_{3/2}\rightarrow{}^4I_{15/2}$ transitions of Er^{3+} ions (the

DOI: 10.1021/acs.inorgchem.9b01570
Inorg. Chem. 2019, 58, 11636−11648

magenta line in Figure 7a). Through monitoring the emission peak at 558 nm, the excitation spectrum of **2** presents three excitation peaks at 268, 378, and 408 nm ascribed to the $^1A_{1g}\rightarrow{}^1T_{1u}$, $^4I_{15/2}\rightarrow{}^4G_{11/2}$, and $^4I_{15/2}\rightarrow{}^4F_{7/2}$ transitions (the pink line in Figure 7a).[64] The overlap of the wide emission band of AT segments and the excitation peaks at 378 and 408 nm of Er^{3+} ions manifests that the occurrence of intramolecular ET process from the $^3T_{1u}\rightarrow{}^1A_{1g}$ transition to the $^4I_{15/2}\rightarrow{}^4G_{11/2}$ and $^4I_{15/2}\rightarrow{}^4F_{7/2}$ transitions. Under the excitation at 408 nm [The excitation upon λ_{ex} = 408 nm comes from the excitation spectrum of **2** (Figure S10b)], the emission spectrum generates two emission peaks at 537 and 558 nm of Er^{3+} ions (Figure 7b). As shown in Figure 7b, the emission intensities of two emission peaks at 537 and 558 nm of Er^{3+} ions upon λ_{ex} = 268 nm is higher than those upon λ_{ex} = 408 nm, which indicates that the emission of Er^{3+} ions can be enhanced under the sensitization of AT segments. The intensity ratio of $I(^2H_{11/2}\rightarrow{}^4I_{15/2})/I(^4S_{3/2}\rightarrow{}^4I_{15/2})$ upon the excitation at 268 nm is 1.16:1.00 while the intensity ratio of $I(^2H_{11/2}\rightarrow{}^4I_{15/2})/I(^4S_{3/2}\rightarrow{}^4I_{15/2})$ upon the excitation at 408 nm is 0.90:1.00, which implies that more energy migrates from the $^3T_{1u}\rightarrow{}^1A_{1g}$ transition to the $^2H_{11/2}\rightarrow{}^4I_{15/2}$ transition and less to the $^4S_{3/2}\rightarrow{}^4I_{15/2}$ transition.

Under the O→W LMCT excitation at 268 nm, TRES of **2** was collected, which displays that the peaks at 470, 537, and 560 nm reach the maximum at 11.4, 11.6, and 11.7 μs, respectively (Figure 7c), finally reduce to the minimum at 39.9, 35.76, and 32.4 μs (Figure 7d) as time goes on. Obviously, the time of emission peaks at 537 and 560 nm reach the maximum is longer than that at 470 nm, which may result from the ET process from AT fragments to Er^{3+} ions.

Moreover, TRES of **2** upon the excitation at 268 nm indicates that the emission intensity at 537 nm is obviously higher than that at 560 nm, and the decay rate of the emission intensity at 537 nm is slower than that at 560 nm. Under the excitation at 408 nm, the emission peak at 537 nm is almost equal to that at 560 nm, and the emission peaks at 537 and 560 nm reach the most at 11.4 and 11.5 μs (Figure 7e) and disappear at 28.5 and 28.0 μs (Figure 7f). TRES of **2** upon the excitation at 408 nm demonstrates that the emission intensity at 537 nm is approximately equal to that at 560 nm, and the decay rate of the emission intensity at 537 nm is slightly faster than that at 560 nm. Two TRES data upon the excitation at 268 and 408 nm indicate that the sensitization of AT segments make the emission peak intensity decay rates of 537 and 560 nm become slightly slow. Furthermore, the observation that the decay rate of the emission intensity at 537 nm upon the excitation at 268 nm is slower than that at 560 nm whereas the decay rate of the emission intensity at 537 nm upon the excitation at 408 nm is slightly faster than that at 560 nm suggests the $^2H_{11/2}\rightarrow{}^4I_{15/2}$ emission acquires more energy than the $^4S_{3/2}\rightarrow{}^4I_{15/2}$ emission.

To explore the ET course from AT segments to Er^{3+} ions in detail, the PL lifetime decay curves of **2** have been also measured upon the excitations at 268 and 408 nm (Figure 8a,b), and related fitting parameters are exhibited in Table S4. Based on the fitting results, under the excitation at 268 nm, the τ^* values are 7.45 and 7.40 μs for the $^2H_{11/2}\rightarrow{}^4I_{15/2}$ and $^4S_{3/2}\rightarrow{}^4I_{15/2}$ emissions, respectively, and the ratio of $\tau^*(^2H_{11/2}\rightarrow{}^4I_{15/2})/\tau^*(^4S_{3/2}\rightarrow{}^4I_{15/2})$ is 1.01:1.00 (Figure 8c). Under the excitation at 408 nm, the τ^* values are 3.79 and 4.11 μs for the $^2H_{11/2}\rightarrow{}^4I_{15/2}$ and $^4S_{3/2}\rightarrow{}^4I_{15/2}$ emissions (Figure 8d), and the ratio of $\tau^*(^2H_{11/2}\rightarrow{}^4I_{15/2})/\tau^*(^4S_{3/2}\rightarrow{}^4I_{15/2})$ is 0.92:1.00. Obviously, the average lifetimes of $^2H_{11/2}\rightarrow{}^4I_{15/2}$ and $^4S_{3/2}\rightarrow{}^4I_{15/2}$ emissions upon the excitation at 268 nm respectively increase by 1.97 and 1.80 times compared to those upon the excitation at 408 nm. It can be also concluded that the $^2H_{11/2}\rightarrow{}^4I_{15/2}$ emission obtains more energy from the $^3T_{1u}\rightarrow{}^1A_{1g}$ emission than the $^4S_{3/2}\rightarrow{}^4I_{15/2}$ emissions upon the excitation at 268 nm. As well, the good energy level match of the $^2H_{11/2}\rightarrow{}^4I_{15/2}$ transition (18.692×10^3 cm^{-1}) energy gap and the $^3T_{1u}\rightarrow{}^1A_{1g}$ transition (21.277×10^3 cm^{-1}) energy gap may lead to the good sensitization degree of AT segments to the $^2H_{11/2}\rightarrow{}^4I_{15/2}$ emission of Er^{3+} ions (Table S6). The schematic ET process from AT segments to Er^{3+} ions in **2** is depicted in Figure 8d. During the O→W LMCT excitation, part energy from the $^3T_{1u}\rightarrow{}^1A_{1g}$ transition of AT segments is reabsorbed by the $^4I_{15/2}\rightarrow{}^4G_{9/2}$, $^4I_{15/2}\rightarrow{}^4G_{11/2}$, and $^4I_{15/2}\rightarrow{}^4F_{7/2}$ transitions of Er^{3+} ions, which prompts the $^2H_{11/2}\rightarrow{}^4I_{15/2}$ and $^4S_{3/2}\rightarrow{}^4I_{15/2}$ transitions.

Based on the above results of PL behaviors in **1** and **2**, it can be summarized that the PL emissions of RE ions in **1** and **2** are sensitized by AT segments. Moreover, the sensitization degree of AT segments to the Dy^{3+} ions is higher than that to Er^{3+} ions.

The CIE 1931 diagram is a well-established method to help understand the authenticity of colors. The chromaticity coordinates can define the precise emission colors of luminescent materials.[42,65] The color represented by the dominant wavelength is theoretically the same as that of a luminescent material. Color purity can be calculated on the basis of eq 3:[42,66]

$$\text{color purity} = [(x - x_i)^2 + (y - y_i)^2/(x_d - x_i)^2 + (y_d - y_i)^2]^{1/2} \quad (3)$$

In eq 3, (x, y) is the color coordinate of the light source, (x_i, y_i) is the coordinate of the white light centered at (0.3333, 0.3333), and (x_d, y_d) is the coordinate involving the dominant wavelength.

The correlated color temperature (CCT) is also an important light factor that can influence subjective feelings in photography, horticulture, and so on.[67,68] CCT can be calculated on the basis of eq 4:

$$\text{CCT} = 499.0n^3 + 3525.0n^2 + 6823.3n + 5520.22 \quad (4)$$

$$n = (x - x_e)/(y_e - y)$$

where x_e (0.3320) and y_e (0.1858) are epicenter coordinates obtained by consecutive tests to minimize the error.[69]

In addition, the chromaticity coordinate of **1** moves from (0.3411, 0.4590) upon the excitation at 450 nm to (0.3153, 0.4035) upon the excitation at 268 nm (Figure 9a). The CIE chromaticity coordinate of **2** shifts from (0.3224, 0.5012) upon the excitation at 408 nm to (0.3478, 0.6084) upon the excitation at 268 nm. It can be observed that the shift of chromaticity coordinates of **1** and **2** toward blue emission under the O→W LMCT excitation relative to those under the *f*–*f* excitation of Dy^{3+} and Er^{3+} ions, which indicates that it is available to tune emission colors via different excitation wavelengths.[70,71] The dominant wavelengths, color purities, and CCT of **1** and **2** are recorded in Table S7.

DOI: 10.1021/acs.inorgchem.9b01570
Inorg. Chem. 2019, 58, 11636−11648

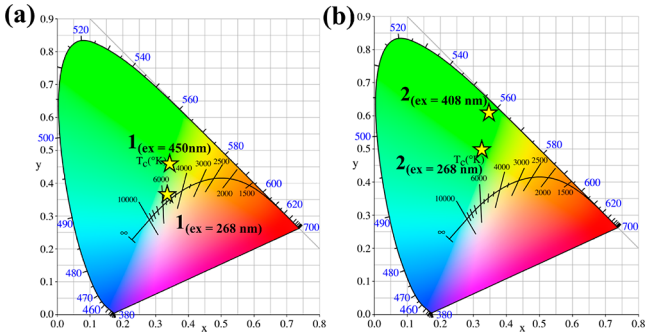

Figure 9. CIE 1931 diagrams of (a) **1** upon the excitation at 268 and 450 nm and (b) **2** upon the excitation at 268 and 408 nm.

CONCLUSIONS

In conclusion, four RE and Sb-oxo-clusters simultaneously bridging tetrameric ATs **1**–**4** were prepared, and their tetrameric polyoxoanions were shown to be constituted by two $[B\text{-}\alpha\text{-}SbW_{10}O_{37}]^{11-}$ and two $[B\text{-}\alpha\text{-}SbW_8O_{31}]^{11-}$ segments and a RE and Sb heterometal $[RE_4(H_2O)_6Sb_6O_4]^{22+}$ cluster. According to the PL measurements, sensitization of AT segments favors the enhancement of emission intensity and the increase of PL lifetime of RE ions in **1** and **2**. Under the sensitization of AT segments, Dy^{3+} ions obtain more energy from AT segments than Er^{3+} ions. In **1**, the $^4F_{9/2}\rightarrow{}^6H_{15/2}$ emission acquires the most energy from O→W LMCT emission, the $^4F_{9/2}\rightarrow{}^6H_{13/2}$ emission is second, and $^4F_{9/2}\rightarrow{}^6H_{11/2}$ emission is the least, while in **2** the $^2H_{11/2}\rightarrow{}^4I_{15/2}$ emission gains more energy than the $^4S_{3/2}\rightarrow{}^4I_{15/2}$ emission. It can be concluded that the great energy level match between the *f*–*f* transition energy gap of RE ions and $^3T_{1u}\rightarrow{}^1A_{1g}$ transition energy gap of AT segments will lead to a strong sensitization effect on the *f*–*f* emission of RE ions. Moreover, CIE diagrams of **1** and **2** show changeable emission colors under O→W LMCT excitation and *f*–*f* excitation of RE ions. In the future, in-depth and systematic investigations on luminescence mechanisms and kinetics of RESHPOTMs will continue to be explored. Furthermore, some functional organic ligands will be also utilized to tune the emission behaviors of RESHPOTMs.

ASSOCIATED CONTENT

Supporting Information

The Supporting Information is available free of charge on the ACS Publications website at DOI: 10.1021/acs.inorgchem.9b01570.

BVS calculations of W, Sb, and RE atoms; related structural figures; PXRD patterns, TG curves, and IR spectra of **1**–**4**; related luminescence spectra and luminescence decay curves, including Figures S1–S12 and Tables S1–S7 (PDF)

Accession Codes

CCDC 1887102–1887104 and 1887206 contain the supplementary crystallographic data for this paper. These data can be obtained free of charge via www.ccdc.cam.ac.uk/data_request/cif, or by emailing data_request@ccdc.cam.ac.uk, or by contacting The Cambridge Crystallographic Data Centre, 12 Union Road, Cambridge CB2 1EZ, UK; fax: +44 1223 336033.

AUTHOR INFORMATION

Corresponding Authors

*E-mail: ljchen@henu.edu.cn.
*E-mail: zhaojunwei@henu.edu.cn.

ORCID

Junwei Zhao: 0000-0002-7685-1309

Notes

The authors declare no competing financial interest.

ACKNOWLEDGMENTS

This work was supported by the Natural Science Foundation of China (21771052, 21671054, 21571048, 21871077), the Innovation Scientists and Technicians Troop Construction Projects of Henan Province (174100510016), the 2014 Special Foundation for Scientific Research Project of Henan University (XXJC20140001), and the 2018 Students Innovative Pilot Plan of Henan University (201810475014).

REFERENCES

(1) Dolbecq, A.; Dumas, E.; Mayer, C. R.; Mialane, P. Hybrid organic-inorganic polyoxometalate compounds: from structural diversity to applications. *Chem. Rev.* **2010**, *110*, 6009–6048.
(2) Zhao, J. W.; Li, Y. Z.; Chen, L. J.; Yang, G. Y. Research progress on polyoxometalate-based transition-metal–rare-earth heterometallic derived materials: synthetic strategies, structural overview and functional applications. *Chem. Commun.* **2016**, *52*, 4418–4445.
(3) Wang, S. S.; Yang, G. Y. Recent advances in polyoxometalate-catalyzed reactions. *Chem. Rev.* **2015**, *115*, 4893–4962.
(4) Wang, Z.; Su, H.-F.; Tung, C.-H.; Sun, D.; Zheng, L.-S. Deciphering synergetic core-shell transformation from $[Mo_6O_{22}@Ag_{44}]$ to $[Mo_8O_{28}@Ag_{50}]$. *Nat. Commun.* **2018**, *9*, 4407.
(5) Mizuno, N.; Yamaguchi, K.; Kamata, K. C. Epoxidation of olefins with hydrogen peroxide catalyzed by polyoxometalates. *Coord. Chem. Rev.* **2005**, *249*, 1944–1956.
(6) Hill, C. L. Progress and challenges in polyoxometalate-based catalysis and catalytic materials chemistry. *J. Mol. Catal. A: Chem.* **2007**, *262*, 2–6.
(7) Zhao, Y.-Q.; Yu, K.; Wang, L.-W.; Wang, Y.; Wang, X.-P.; Sun, D. Anion-induced supramolecular isomerism in two preyssler P_5W_{30} polyoxometalate-based hybrid materials. *Inorg. Chem.* **2014**, *53*, 11046–11050.
(8) Misra, A.; Castillo, I. F.; Müller, D. P.; González, C.; Eyssautier-Chuine, S.; Ziegler, A.; de la Fuente, J. M.; Mitchell, S. G.; Streb, C. Polyoxometalate-ionic liquids (POM-ILs) as anticorrosion and antibacterial coatings for natural stones. *Angew. Chem., Int. Ed.* **2018**, *57*, 14926–14931.
(9) Marrot, J.; Pilette, M. A.; Haouas, M.; Floquet, S.; Taulelle, F.; Lopez, X.; Poblet, J. M.; Cadot, E. Polyoxometalates paneling through $\{Mo_2O_2S_2\}$ coordination: cation-directed conformations and chemistry of a supramolecular hexameric scaffold. *J. Am. Chem. Soc.* **2012**, *134*, 1724–1737.
(10) Liu, J.-W.; Feng, L.; Su, H.-F.; Wang, Z.; Zhao, Q.-Q.; Wang, X.-P.; Tung, C. – H.; Sun, D. Anisotropic assembly of Ag_{52} and Ag_{76} nanoclusters. *J. Am. Chem. Soc.* **2018**, *140*, 1600–1603.
(11) Ma, F. J.; Liu, S. X.; Sun, C. Y.; Liang, D. D.; Ren, G. J.; Wei, F.; Chen, Y. G.; Su, Z. M. A sodalite-type porous metal-organic framework with polyoxometalate templates: adsorption and decomposition of dimethyl methylphosphonate. *J. Am. Chem. Soc.* **2011**, *133*, 4178–4181.
(12) Chakraborty, B.; Gan-Or, G.; Duan, Y.; Raula, M.; Weinstock, I. A. Visible-light-driven water oxidation with a polyoxometalate -complexed hematite core of 275 iron atoms. *Angew. Chem., Int. Ed.* **2019**, *58*, 6584–6589.
(13) Iqbal, A.; Asif, H. M.; Zhou, Y. S.; Zhang, L. J.; Wang, T.; Shehzad, F. K.; Ren, X. Y. From simplicity to complexity in grafting Dawson-type polyoxometalates on porphyrin, leading to the

DOI: 10.1021/acs.inorgchem.9b01570
Inorg. Chem. 2019, 58, 11636–11648

formation of new organic−inorganic hybrids for the investigation of third-order optical nonlinearities. *Inorg. Chem.* **2019**, *58*, 8763−8774.
(14) Blazevic, A.; Rompel, A. The Anderson−Evans polyoxometalate: from inorganic building blocks via hybrid organic−inorganic structures to tomorrows "bio-POM. *Coord. Chem. Rev.* **2016**, *307*, 42−64.
(15) Li, Y.-W.; Guo, L.-Y.; Su, H.-F.; Jagodič, M.; Luo, M.; Zhou, X.-Q.; Zeng, S.-Y.; Tung, C.-H.; Sun, D. Two unprecedented POM-based inorganic−organic hybrids with concomitant hetero- polytungstate and molybdate. *Inorg. Chem.* **2017**, *56*, 2481−2489.
(16) Liu, H.; Qin, C.; Wei, Y. G.; Xu, L.; Gao, G. G.; Li, F. Y.; Qu, X. S. Copper-complex-linked polytungstobismuthate (-antimonite) chain containing sandwich Cu(II) ions partially modified with imidazole ligand. *Inorg. Chem.* **2008**, *47*, 4166−4172.
(17) Raula, M.; Gan Or, G.; Saganovich, M.; Zeiri, O.; Wang, Y.; Chierotti, M. R.; Gobetto, R.; Weinstock, I. A. Polyoxometalate complexes of anatase-titanium dioxide cores in water. *Angew. Chem., Int. Ed.* **2015**, *54*, 12416−12421.
(18) Yan, B.-J.; Du, X.-S.; Huang, R.-W.; Yang, J.-S.; Wang, Z.-Y.; Zang, S.-Q.; Mak, T. C. W. Self-assembly of a stable silver thiolate nanocluster encapsulating a lacunary Keggin phosphotungstate anion. *Inorg. Chem.* **2018**, *57*, 4828−4832.
(19) Ritchie, C.; Moore, E. G.; Speldrich, M.; Kögerler, P.; Boskovic, C. Terbium polyoxometalate organic complexes: correlation of structure with luminescence properties. *Angew. Chem., Int. Ed.* **2010**, *49*, 7702−7871.
(20) Reinoso, S.; Giménez-Marqués, M.; Galán-Mascarós, J. R.; Vitoria, P.; Gutiérrezzorrilla, J. M. Giant crown-shaped polytungstate formed by self-assembly of Ce^{III} stabilized dilacunary Keggin fragments. *Angew. Chem., Int. Ed.* **2010**, *49*, 8384−8388.
(21) Miras, H. N.; Yan, J.; Long, D. L.; Cronin, L. Engineering polyoxometalates with emergent properties. *Chem. Soc. Rev.* **2012**, *41*, 7403−7430.
(22) Reinoso, S.; Galánmascarós, J. R.; Lezama, L. New type of heterometallic 3d-4f rhomblike core in Weakley-like polyoxometalates. *Inorg. Chem.* **2011**, *50*, 9587−9598.
(23) Reinoso, S.; Galánmascarós, J. R. Heterometallic 3d-4f polyoxometalate derived from the Weakley-type dimeric structure. *Inorg. Chem.* **2010**, *49*, 377−379.
(24) Ibrahim, M.; Mereacre, V.; Leblanc, N.; Wernsdorfer, W.; Anson, C. E.; Powell, A. K. Self-assembly of a giant tetrahedral 3d−4f single-molecule magnet within a polyoxometalate system. *Angew. Chem., Int. Ed.* **2015**, *54*, 15574−15578.
(25) Chen, L. J.; Cao, J.; Li, X. H.; Ma, X.; Luo, J.; Zhao, J. W. The first purely inorganic polyoxotungstates constructed from dimeric tungstoantimonate-based iron−rare-earth heterometallic fragments. *CrystEngComm* **2015**, *17*, 5002−5013.
(26) Zhao, J. W.; Li, Y. Z.; Ji, F.; Yuan, J.; Chen, L. J.; Yang, G. Y. Syntheses, structures and electrochemical properties of a class of 1-D double chain polyoxotungstate hybrids $[H_2dap][Cu(dap)_2]_{0.5}$ $[Cu(dap)_2(H_2O)][Ln(H_2O)_3(\alpha\text{-}GeW_{11}O_{39})]\cdot 3H_2O$. *Dalton Trans.* **2014**, *43*, 5694−5706.
(27) Xue, G.; Vaissermann, J.; Gouzerh, P. Cerium(III) complexes with lacunary polyoxotungstates synthesis and structural characterization of a novel heteropolyoxotungstate based on $a\text{-}[SbW_9O_{33}]^{9-}$ units. *J. Cluster Sci.* **2002**, *13*, 409−421.
(28) Artetxe, B.; Reinoso, S.; San Felices, L.; Lezama, L.; Gutierrez-Zorrilla, J. M.; Vicent, C.; Haso, F.; Liu, T. New perspectives for old clusters: Anderson-Evans anions as building blocks of large polyoxometalate frameworks in a series of heterometallic 3d−4f species. *Chem. - Eur. J.* **2016**, *22*, 4616−4625.
(29) Cai, J.; Zheng, X. Y.; Xie, J.; Yan, Z. H.; Kong, X. J.; Ren, Y. P.; Long, L. S.; Zheng, L. S. Anion-dependent assembly of heterometallic 3d−4f clusters based on a lacunary polyoxometalate. *Inorg. Chem.* **2017**, *56*, 8439−8445.
(30) Liu, J. L.; Jin, M. T.; Chen, L. J.; Zhao, J. W. First dimethyltin-functionalized rare-earth incorporated tellurotungstates consisting of $\{B\text{-}\alpha\text{-}TeW_7O_{28}\}$ and $\{W_5O_{18}\}$ mixed building units. *Inorg. Chem.* **2018**, *57*, 12509−12520.
(31) Nohra, B.; Mialane, P.; Dolbecq, A.; Rivière, E.; Marrot, J.; Sécheresse, F. Heterometallic 3d−4f cubane clusters inserted in polyoxometalate matrices. *Chem. Commun.* **2009**, *40*, 2703−2705.
(32) Hu, T.-P.; Zhao, Y.-Q.; Jaglicič, Z.; Yu, K.; Wang, X. − P.; Sun, D. Four hybrid materials based on preyssler P_5W_{30} polyoxometalate and first-row transition-metal complex. *Inorg. Chem.* **2015**, *54*, 7415−7423.
(33) Reinoso, S. Heterometallic 3d−4f polyoxometalates: still an incipient field. *Dalton Trans.* **2011**, *40*, 6610−6615.
(34) Artetxe, B. Systematic studies on 3d- and 4f-metal containing polyoxometalates suitable for organic derivatization. *ChemistryOpen* **2016**, *5*, 261−266.
(35) Zhang, J.; Cai, G. M.; Yang, L. W.; Ma, Z. Y.; Jin, Z. P. Layered crystal structure, color-tunable photoluminescence, and excellent thermal stability of $MgIn_2P_4O_{14}$ phosphate-based phosphors. *Inorg. Chem.* **2017**, *56*, 12902−12913.
(36) Chen, Y. H.; Sun, L. H.; Chang, S. Z.; Chen, L. J.; Zhao, J. W. Synergistic effect between different coordination geometries of lanthanides and various coordination modes of 2-picolinic acid ligands tuning three types of rare 3d−4f heterometallic tungstoantimonates. *Inorg. Chem.* **2018**, *57*, 15079−15092.
(37) Wu, H.; Yan, B.; Li, H.; Singh, V.; Ma, P.; Niu, J.; Wang, J. Enhanced photostability luminescent properties of Er^{3+}-doped near-white-emitting $Dy_xEr_{(1-x)}$-POM derivatives. *Inorg. Chem.* **2018**, *57*, 7665−7675.
(38) Singh, N. S.; Sahu, N. K.; Bahadur, D. Multicolor tuning and white light emission from lanthanide doped $YPVO_4$ nanorods: energy transfer studies. *J. Mater. Chem. C* **2014**, *2*, 548−555.
(39) Yamase, T. Photo- and electrochromism of polyoxometalates and related materials. *Chem. Rev.* **1998**, *98*, 307.
(40) Ritchie, C.; Baslon, V.; Moore, E. G.; Reber, C.; Boskovic, C. Sensitization of lanthanoid luminescence by organic and inorganic ligands in lanthanoid-organic-polyoxometalates. *Inorg. Chem.* **2012**, *51*, 1142−1151.
(41) Han, Q.; Wen, Y.; Liu, J. C.; Zhang, W.; Chen, L. J.; Zhao, J. W. Rare-earth-incorporated tellurotungstate hybrids functionalized by2-picolinic acid ligands: syntheses, structures, and properties. *Inorg. Chem.* **2017**, *56*, 13228−13240.
(42) Li, H. L.; Liu, Y. J.; Liu, J. L.; Chen, L. J.; Zhao, J. W.; Yang, G. Y. Structural transformation from dimerization to tetramerization of serine-decorated rare-earth-incorporated arsenotungstates induced by the usage of rare-earth salts. *Chem. - Eur. J.* **2017**, *23*, 2673−2689.
(43) Bi, L. H.; Al-Kadamany, G.; Chubarova, E. V.; Dickman, M. H.; Chen, L.; Gopala, D. S.; Richards, R. M.; Keita, B.; Nadjo, L.; Jaensch, H.; Mathys, G.; Kortz, U. Organo-ruthenium supported heteropolytungstates: synthesis, structure, electrochemistry, and oxidation catalysis. *Inorg. Chem.* **2009**, *48*, 10068−10077.
(44) Kalinina, I. V.; Izarova, N. V.; Kortz, U. Bis[tetraruthenium (IV)]-containing polyoxometalates: $[\{Ru^{IV}_4O_6(H_2O)_9\}_2Sb_2W_{20}O_{68}(OH)_2]^{4-}$ and $[\{Ru^{IV}_4O_6(H_2O)_9\}_2\{Fe(H_2O)_2\}_2\{\beta\text{-}TeW_9O_{33}\}_2H]^{-}$. *Inorg. Chem.* **2012**, *51*, 7442−7444.
(45) Zhao, C.; Kambara, C. S.; Yang, Y.; Kaledin, A. L.; Musaev, D. G.; Lian, T.; Hill, C. L. Synthesis, structures, and photochemistry of tricarbonyl metal polyoxoanion complexes, $[X_2W_{20}O_{70}\{M(CO)_3\}_2]^{12-}$ (X = Sb, Bi and M = Re, Mn). *Inorg. Chem.* **2013**, *52*, 671−678.
(46) Artetxe, B.; Reinoso, S.; San Felices, L.; Lezama, L.; Pache, A.; Vicent, C.; Gutierrez-Zorrilla, J. M. Rearrangement of a Krebs-type polyoxometalate upon coordination of N,O-bis(bidentate) ligands. *Inorg. Chem.* **2015**, *54*, 409−411.
(47) Chen, W. C.; Yan, L. K.; Wu, C. X.; Wang, X. L.; Shao, K. Z.; Su, Z. M.; Wang, E. B. Assembly of Keggin-/Dawson-type polyoxotungstate clusters with different metal units and SeO_3^{2-} heteroanion templates. *Cryst. Growth Des.* **2014**, *14*, 5099−5110.
(48) Haider, A.; Ibrahim, M.; Bassil, B. S.; Carey, A. M.; Viet, A. N.; Xing, X.; Ayass, W. W.; Minambres, J. F.; Liu, R.; Zhang, G.; Keita, B.; Mereacre, V.; Powell, A. K.; Balinski, K.; N'Diaye, A. T.; Kupper, K.; Chen, H.-Y.; Stimming, U.; Kortz, U. Mixed-valent Mn_{16}-containing

DOI: 10.1021/acs.inorgchem.9b01570
Inorg. Chem. 2019, 58, 11636−11648

heteropolyanions: tuning of oxidation state and associated physicochemical properties. *Inorg. Chem.* **2016**, *55*, 2755−2764.
(49) Zhang, Z.; Wang, Y. L.; Yang, G. Y. An unprecedented Zr-containing polyoxometalate tetramer with mixed trilacunary/dilacunary Keggin type polyoxotungstate units. *Acta Crystallogr., Sect. C: Struct. Chem.* **2018**, *C74*, 1284−1288.
(50) Zhao, J. W.; Cao, J.; Li, Y. Z.; Zhang, J.; Chen, L. J. First tungstoantimonate-based transition-metal−lanthanide heterometallic hybrids functionalized by amino acid ligands. *Cryst. Growth Des.* **2014**, *14*, 6217−6229.
(51) Zhang, Y.; Liu, X.; Lang, Y.; Yuan, Z.; Zhao, D.; Qin, G.; Qin, W. Synthesis of ultra-small $BaLuF_5$:Yb^{3+}, Er^{3+}@$BaLuF_5$:Yb^{3+} active-core− active shell nanoparticles with enhanced up-conversion and down-conversion luminescence by a layer-by-layer strategy. *J. Mater. Chem. C* **2015**, *3*, 2045−2053.
(52) Wu, Y. M.; Cen, Y.; Huang, L. J.; Yu, R. Q.; Chu, X. Upconversion fluorescence resonance energy transfer biosensor for sensitive detection of human immunodeficiency virus antibodies in human serum. *Chem. Commun.* **2014**, *50*, 4759−4762.
(53) Zhang, J.; Hong, G. Synthesis and photoluminescence of the Y_2O_3: Eu^{3+} phosphor nanowires in AAO template. *J. Solid State Chem.* **2004**, *177*, 1292−1296.
(54) Guan, H.; Sheng, Y.; Song, Y.; Xu, C.; Zhou, X.; Zheng, K.; Shi, Z.; Zou, H. YF_3:RE^{3+} (RE = Dy, Tb, Eu) Sub-microstructures: controllable morphology, tunable multicolor, and thermal properties. *J. Phys. Chem. C* **2017**, *121*, 23080−23095.
(55) Min, X.; Huang, Z.; Fang, M.; Liu, Y.; Tang, C.; Wu, X. Energy transfer from Sm^{3+} to Eu^{3+} in red-emitting phosphor $LaMgAl_{11}O_{19}$:Sm^{3+}, Eu^{3+} for solar cells and near-ultraviolet white light-emitting diodes. *Inorg. Chem.* **2014**, *53*, 6060−6065.
(56) Liu, Y.; Liu, G. X.; Wang, J. X.; Dong, X. T.; Yu, W. S. Single-component and warm-white-emitting phosphor $NaGd(WO_4)_2$:Tm^{3+}, Dy^{3+}, Eu^{3+}: synthesis, luminescence, energy transfer, and tunable color. *Inorg. Chem.* **2014**, *53*, 11457−11466.
(57) Zhang, Y.; Gong, W. T.; Yu, J. J.; Pang, H. C.; Song, Q.; Ning, G. L. Tunable white-light emission via energy transfer in single-phase $LiGd(WO_4)_2$:RE^{3+} (RE = Tm, Tb, Dy, Eu) phosphors for UV-excited WLEDs. *RSC Adv.* **2015**, *5*, 96272−96280.
(58) Yu, C. Y.; Yang, Z. W.; Huang, A. J.; Chai, Z. Z.; Qiu, J. B.; Song, Z. G.; Zhou, D. C. Photoluminescence properties of tellurite glasses doped Dy^{3+} and Eu^{3+} for the UV and blue converted WLEDs. *J. Non-Cryst. Solids* **2017**, *457*, 1−8.
(59) Fu, Z. L.; Xia, W. W.; Li, Q. S.; Cui, X. Y.; Li, W. H. Highly uniform $NaLa(MoO_4)_2$:Ln^{3+} (Ln = Eu, Dy) microspheres: template free hydrothermal synthesis, growing mechanism, and luminescent properties. *CrystEngComm* **2012**, *14*, 4618−4624.
(60) Li, P. L.; Wang, Z. J.; Yang, Z. P.; Guo, Q. L. Tunable blue−green emission phosphor Ca_2PO_4Cl:Ce^{3+},Tb^{3+}: luminescence and energy transfer. *Opt. Commun.* **2014**, *332*, 83−88.
(61) Zhou, J.; Xia, Z. G. Luminescence color tuning of Ce^{3+}, Tb^{3+} and Eu^{3+} codoped and tri-doped $BaY_2Si_3O_{10}$ phosphors via energy transfer. *J. Mater. Chem. C* **2015**, *3*, 7552−7560.
(62) Li, G. Z.; Wang, Z. L.; Yu, M.; Quan, Z. W.; Lin, J. Fabrication and optical properties of core−shell structured spherical SiO_2@$GdVO_4$: Eu^{3+} phosphors via sol−gel process. *J. Solid State Chem.* **2006**, *179*, 2698−2706.
(63) Wei, T.; Tian, Y.; Tian, C.; Cai, M. Z.; Jing, X. F.; Li, B. P.; Chen, R.; Zhang, J. J.; Xu, S. Q. Quantitative analysis of energy transfer and origin of quenching in Er^{3+}/Ho^{3+} codoped germanosilicate glasses. *J. Phys. Chem. A* **2015**, *119*, 6823−6830.
(64) Cichos, J.; Marciniak, L.; Hreniak, D.; Strek, W.; Karbowiak, M. The effect of surface ligand, solvent and Yb^{3+} codoping on the luminescence properties of Er^{3+} in colloidal $NaGdF_4$ nanocrystals. *J. Mater. Chem. C* **2014**, *2*, 8244−8251.
(65) Zhang, Y.; Gong, W.; Yu, J.; Pang, H.; Song, Q.; Ning, G. A new single -phase white-light-emitting $CaWO_4$:Dy^{3+} phosphor: synthesis, luminescence and energy transfer. *RSC Adv.* **2015**, *5*, 62527−62533.
(66) Kumar, J. S.; Pavani, K.; Babu, A. M.; Giri, N. K.; Rai, S. B.; Moorthy, L. R. Fluorescence characteristics of Dy^{3+} ions in calcium fluoroborate glasses. *J. Lumin.* **2010**, *130*, 1916−1923.
(67) Wang, Q.; Xu, H. S.; Zhang, F. Z.; Wang, Z. H. Influence of color temperature on comfort and preference for LED indoor lighting. *Optik* **2017**, *129*, 21−29.
(68) Kapogiannatou, A.; Paronis, E.; Paschidis, K.; Polissidis, A.; Kostomitsopoulos, N. G. Effect of light colour temperature and intensity on τhε behaviour of male C57CL/6J mice. *Appl. Anim. Behav. Sci.* **2016**, *184*, 135−140.
(69) McCamy, C. S. Correlated color temperature as an explicit function of chromaticity coordinates. *Color Res. Appl.* **1992**, *17*, 142−144.
(70) Wu, H. C.; Wan, R.; Si, Y. N.; Ma, P. T.; Wang, J. P.; Niu, J. Y. A helical chain-like organic−inorganic hybrid arsenotungstate with color-tunable photoluminescence. *Dalton Trans.* **2018**, *47*, 1958−1965.
(71) Zhang, Q. W.; Li, D. F.; Li, X.; White, P. B.; Mecinovic, J.; Ma, X.; Ågren, H.; Nolte, R. J. M.; Tian, H. Multicolor photoluminescence includizng white-light emission by a single host-guest complex. *J. Am. Chem. Soc.* **2016**, *138*, 13541−13550.

DOI: 10.1021/acs.inorgchem.9b01570
Inorg. Chem. 2019, 58, 11636−11648